Polymer Testing 87 (2020) 106548

Contents lists available at ScienceDirect

Polymer Testing

journal homepage: http://www.elsevier.com/locate/polytest

Test Method

A new theoretical-experimental model deriving from the contactless measurement of the thickness of bulge-tested elastomeric samples

F. Lo Savio [a,*], G. La Rosa [a], M. Bonfanti [b]

[a] Dept. of Civil Engineering and Architecture, Univ. of Catania, Via S. Sofia, 54, 95100, Catania, Italy
[b] Dept. of Electrical, Electronic and Informatics Engineering, Univ. of Catania, Via S. Sofia, 54, 95100, Catania, Italy

ARTICLE INFO

Keywords:
Contactless ultrasonic measurement
Acoustoelastic effect
Bulge test
Dome apex thickness
Hyperelastic materials

ABSTRACT

In this paper, an ultrasound measurement method was applied to bulge test on carbon black-filled SBR specimens, in order to determine their thickness at the top of the dome. This method consists in measuring first the variation in the ultrasonic velocity as a function of the deformation in the uniaxial state and subsequently obtaining the thickness value in the equibiaxial state, assuming the congruence of velocity in uniaxial and equibiaxial stress states, respectively.

The comparison between experimental data and the thickness values deriving from the most reliable theoretical criteria for both metallic and rubbers-like materials was shown.

A new theoretical approach taking into account the slight compressibility of elastomers to estimate the thickness at the dome apex was proposed. Such an approach provided a general equation to define the thickness of the dome in bulge-tested SBR+20%CB as a function of the Poisson ratio.

1. Introduction

The characterization of rubber-like materials requires the knowledge of numerous parameters necessary to define their strongly non-linear mechanical behavior [1–6]. Therefore, several techniques are used to obtain the stress-strain relation, such as uniaxial tensile-compressive, planar, equibiaxial, indentation and hydraulic bulge tests. Usually, the results derived from coupled tests have to be combined to define these hyperelastic parameters [7,8]. In fact, the universally adopted uniaxial tensile test is not enough to characterize materials subjected to biaxial stress conditions, such as tubes or membranes. Since many years the bulge test is a consolidate technique for the investigation of membranes under equibiaxial tension state. Furthermore, this method can eliminate edge damages that may occur when the specimen is uniaxially stressed [9].

The hydraulic inflation test, where a material thin sheet of uniform thickness is clamped over a cavity and subjected to unilateral fluid pressure causing the sheet to bulge plastically assuming a semi-spherical shape, was developed specifically to determine the flow stress curves during sheet metal forming operations [10–12]. Stress conditions in such a test are equibiaxial at the apex of the sample dome. Although tensile testing of metal alloys at high temperatures is an easy and cheap technique, it involves the drawback of deforming the specimens in only one direction, whereas the real forming process produces a biaxial stress state [13]. On the other hand, the bulging technique is characterized by the need to find the relation between the pressure-displacement and stress-strain curves. Since in isotropic materials the stress state is equibiaxial on the whole dome, this relationship is unique [14]. Consequently, this technique can be extended also to rubber-like materials, which are typically isotropic if not subjected to the calendering process [15,16].

To obtain the stress-strain curve as a function of inflation pressure it is important that values of the thickness and height of the dome are known [17–19]. Many researchers developed different analytical approaches to estimate the value of the thickness at the top of thin metal specimens, basing on the restrictive assumptions of the incompressibility and perfect isotropy of the tested material [20–27].

All above mentioned analytical approaches require the direct measurement of the height of the dome. Over the years, this measure has been refined by replacing direct contact techniques, performed with mechanical transducers (comparators [14], extensometers [28] and LVDT [29]), with optical contactless techniques (retro-reflection laser [11,30,31] and interferometers [32–35]).

Requiring the effective measurement of the height of the dome to

* Corresponding author.
E-mail address: flosavio@dii.unict.it (F. Lo Savio).

https://doi.org/10.1016/j.polymertesting.2020.106548
Received 8 January 2020; Received in revised form 28 March 2020; Accepted 6 April 2020
Available online 13 April 2020

obtain analytically the value of the thickness, all the procedures described are called *indirect measurement methods* [36].

Further indirect methods exploit the three-dimensional reconstruction to derive some geometric parameters of the dome as the inflation pressure changes. The main parameters are stretches in the meridional and circumferential directions, from which to derive the meridional and circumferential strains, respectively, and the height and thickness at the top of the dome [25,37]. To obtain a faithful reconstruction of the dome, techniques focused on epipolar geometry [7,17,19], on 3D-Digital Image Correlation [13,38,39] and, recently, implemented with neural networks [40] were adopted.

Nevertheless, the effective measurement of both the thickness and height at the apex of the dome under deformed conditions would be desirable. *Direct measurement methods* using acoustic transducers have recently been introduced on this need. A first attempt was made by Marinho et al., who used contact ultrasonic sensors placed on thin metal plates exploiting the pulse-echo method [36].

Theoretical studies to derive the thickness as a function of the inflating pressure, under the same assumptions imposed on metals, were also carried out on rubbers and soft materials [41–44]. However, the application of such different approaches involves some considerable differences in the obtained values of mechanical properties for the same material [9]. Furthermore, the use of the bulge test method to measure the hyperelastic parameters of thin and soft membranes at large deformations is not reliable due to the strongly non-linear behavior [45].

To overcome these problems, direct knowledge of the height and thickness of the dome is essential. Although obtaining reliable results, the above described contact ultrasonic technique [36] is not suitable for soft materials and elastomers, generating non-negligible instrument insertion errors.

In this paper, a new direct method for measuring the thickness and height of the dome in elastomeric sheets under bulging, based on a non-contact ultrasonic technique, was proposed.

Moreover, from experimental results an alternative theoretical approach to estimate the thickness at the dome apex was suggested. Unlike theoretical models proposed in the scientific literature, this approach takes into account the slight volume change of elastomers while inflating.

2. Theoretical background

2.1. Bulge test

The bulge test requires a simple equipment consisting essentially in a fluid pumping system, a pressure transducer and a measurement system to continuously monitor geometrical parameters of the dome as inflating pressure changes.

In addition to the previously mentioned assumptions of isotropy, incompressibility and semi-spherical bulging of the sample, the inflation test needs that the strain rate is so slow to make inertial forces negligible and the specimen thickness is small compared to the curvature radius of the dome.

Under these assumptions, the stress state can be considered as plane and equibiaxial, allowing the application of the Boyle-Mariotte law, valid for thin-walled tanks:

$$\sigma_c = \sigma_m = \frac{p \cdot R}{2 \cdot s} \tag{1}$$

where σ_c and σ_m are the circumferential and meridional stress, respectively, s is the thickness at the apex of the dome, R is the curvature radius of the assumed spherical dome, and p is the inflating pressure (Fig. 1).

At the apex of the dome each meridian is a principal direction and the stress state is equibiaxial. Therefore, on the bulge surface the true principal strains are equal ($\varepsilon_1 = \varepsilon_2$). From the knowledge of both the undeformed l_0 and the deformed length l_d of a membrane element

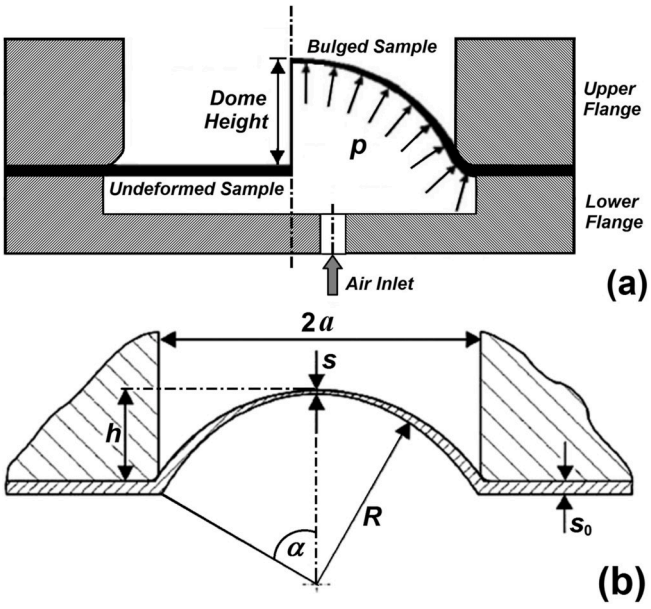

Fig. 1. (a) Bulge test scheme. (b) Main geometrical parameters.

(Fig. 2), these strains are [7]:

$$\varepsilon_1 = \varepsilon_2 = ln\frac{l_d}{l_0} \tag{2}$$

As stated before, by considering constant volume law ($\varepsilon_1 + \varepsilon_2 + \varepsilon_3 = 0$):

$$\varepsilon_1 = \varepsilon_2 = -\frac{\varepsilon_3}{2} \tag{3}$$

and from the equation of equivalent strain ($\bar{\varepsilon}$) according to Von Mises's criterion:

$$\bar{\varepsilon} = \frac{\sqrt{2}}{3}\sqrt{(\varepsilon_1 - \varepsilon_3)^2 + (\varepsilon_1 - \varepsilon_2)^2 + (\varepsilon_3 - \varepsilon_2)^2} \tag{4}$$

From (3) and (4) the through-thickness strain (ε_3) can be derived [7]:

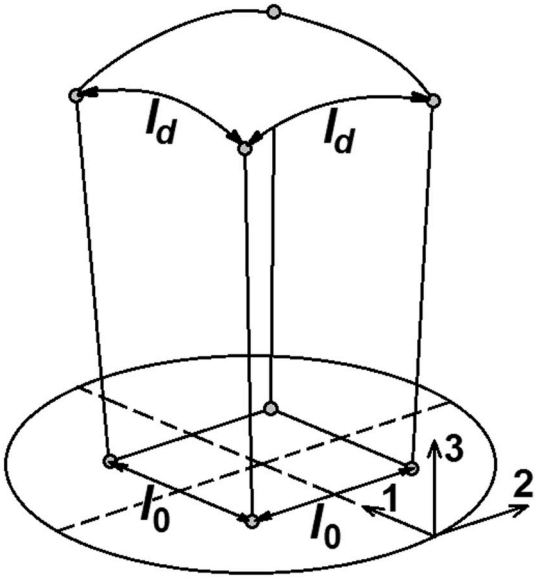

Fig. 2. Undeformed and deformed lengths of a membrane element.

$$\bar{\varepsilon} = -\varepsilon_3 = ln\frac{s_0}{s} \tag{5}$$

where s_0 is the thickness of the undeformed membrane.

The assumption of spherical geometry of the dome while the deformation changes implies that:

$$R = \frac{a^2 + h^2}{2h} \tag{6}$$

where h is the height at the top of the dome and a is the radius of the bulging chamber (Fig. 1b).

2.2. Analytical models for the thickness at the dome apex

As previously stated, indirect measurement methods require the use of theoretical-experimental models to estimate the thickness at the top of the dome. The first theoretical approaches were developed for thin metal plates.

In the elastic-linear field ($\sigma = E\varepsilon$), the through-thickness strain, described by (5), can be expressed in the form:

$$s = s_0 e^{-\varepsilon_3} \tag{7}$$

At higher deformations, after initial yield point, the stress-strain curve assumes a plastic behavior that can be expressed by the following power law:

$$\sigma = K\varepsilon^n \tag{8}$$

where K is the material strength coefficient and n is the strain-hardening index [46].

Hill [20] and later Marciniak [22,47], assuming a spherical shape dome, proposed a law on thinning of the thickness not including the n-index:

$$s = s_0 \left[\frac{1}{1 + \left(\frac{h}{a}\right)^2}\right]^2 \tag{9}$$

In the assumptions of volume constancy and absence of hardening work, Jovane determined the following model [21]:

$$s = s_0 \left[\frac{1}{1 + \left(\frac{h}{a}\right)^2}\right] \tag{10}$$

Kruglov et al. imposed the incompressibility of the material according to the Lagrangian approach and derived a new geometric model based on the convective system of coordinates of a point of the continuum [27]. With the notations of Fig. 1b, this model at the apex of the dome takes the form:

$$s = s_0 \left(\frac{sin\alpha}{\alpha}\right)^2 = s_0 \left[\frac{\frac{a}{R}}{sin^{-1}\left(\frac{a}{R}\right)}\right]^2 \tag{11}$$

where $\alpha = arcsin(a/R)$.

Shang and Shim proposed a modified model taking the fillet on the upper flange of the bulge chamber into account [24]. With reference to Fig. 3, the radius of the dome (R) becomes:

$$R = \frac{h^2 + \bar{a}^2}{2h} - \delta \tag{12}$$

Chakrabarty and Alexander [23] considered the hardening effect on the material thinning and, thus, modified Eq. (9) by Hill-Marciniak:

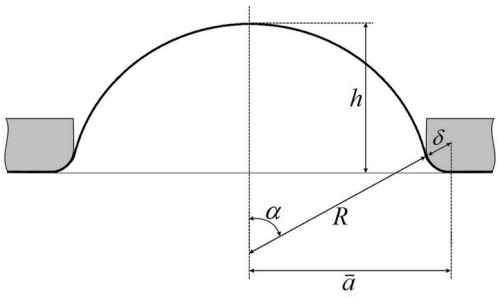

Fig. 3. Shang and Shim bulge-test scheme.

$$s = s_0 \left[\frac{1}{1 + \left(\frac{h}{a}\right)^2}\right]^{2-n} \tag{13}$$

As confirmation of the Chakrabarty and Alexander intuition, Gutscher et al. [10] proved n-index to be the unique parameter influencing the thickness trend, through a numerical-iterative computation based on Eq. (9).

Some of the most widely used theoretical models related to the metal forming process are summarized in the works of Slota and Spišak [48] and Koç et al. [11].

Nowadays, in the scientific literature related to the bulge test on elastomers and soft materials it is not possible to find an equally large number of analytical models.

Adopting the assumptions already described for metals, Reuge et al. obtained the following formulation for rubber-like materials [42]:

$$s = s_0 \frac{a^2}{\left(\frac{a^2+h^2}{2h}\right)^2 arccos^2\left(1 - \frac{2h^2}{a^2+h^2}\right)} \tag{14}$$

with the same notations of Fig. 1b.

However, considering the (6) relationship, the equipollence between Eq. (14) and Eq. (11) by Kruglov et al. [27] can be demonstrated via simple mathematical passages.

Another model on the behavior of the thickness at the dome apex, based on the assumption of quasi-incompressible material [49–51], was introduced by Charalambides et al. testing a soft material (flour and water dough) [44]. This hypothesis implies that the Poisson ratio is less than 0.5 (incompressible material). Applying the Hooke law to biaxial case and considering $\nu = 0.46$, Charalambides et al. obtained:

$$\varepsilon_3 = -\frac{2\nu}{1-\nu}\varepsilon_1 = -1.704\ \varepsilon_1 \tag{15}$$

Therefore, according to Eq. (7), the thickness at the top of the dome was:

$$s = s_0 e^{-1.704\varepsilon_1} \tag{16}$$

3. Materials and methods

In this paper, the authors proposed a device for the direct measurement of the thickness at the dome apex of an isotropic elastomeric material subjected to bulge test. Since the sheets of rubber-like materials available on the market are made by calendering, they exhibit a slight transverse isotropy [16,17,51]. Therefore, the authors obtained sheets of isotropic material by subjecting a compound vulcanized in the laboratory to the hot-pressing technique.

3.1. Tested rubber-like material

The material selected for the inflation test was an elastomer extensively used in the automotive tires industry: the carbon black (CB) filled Styrene-Butadiene Rubber (SBR). This elastomer was previously characterized on commercial calendered sheets in some papers of the authors [31,40,51,52].

The compound SBR1502 filled with CB (N220) in 20% percentage was prepared according to ASTM 3812–16 [52–55]. A lab two-roll mill was used to perform mixing and mastication operations. The mixing operation consisted of two-steps: *master batch* and *final batch*. The first stage was obtained by adding cure activators (ZnO and Stearic Acid), antioxidant (TMQ) and antiozonant (6PPD) to SBR-CB batch. After storage for 36 h at room temperature, the master batch was compounded with vulcanization agents (Sulfur) and accelerators (TBBS) on the two-roll mill, at a working temperature of 50 °C. The composition is shown in Table 1. The final batch thus obtained was hot-pressed at 160 °C for a curing time (t_{100}) of 10:27 (min:sec) in order to carry out good filler flocculation and rubber vulcanization [56]. The optimum value for t_{100} was determined from the rheocurve (Torque-Time) obtained using an oscillating disk rheometer according to the ASTM D5289-19 test method [53,55].

From one of those sheets (thickness $s = 3.02$ mm) specimens shaped straight section and size 25 × 110 mm^2 were cut. Three of these samples were tensile-tested using a Zwick-Roell Z-100 machine, in accordance with the ASTM D412-16. The precision of values measured in the tensile-test, that is equal to the mean values measured on the three specimens, was in accordance with the ASTM D4483-18 requirements.

In addition to the shaped straight section samples to be used in the uniaxial tensile-tests involved by the direct method described on this paper, five square samples (180 × 180 mm^2) to be used for bulge tests were cut from the same sheet.

Fig. 4 shows the specimens used in the uniaxial tensile-test and inflation test. On the rectangular-shape samples (Fig. 4a), the silk-screened lines indicating the two grip zones, the length of the gage and the transverse median are noted. The grid screen-printed on the bulge test samples (Fig. 4b) consists of 5 concentric circles, a small central circle corresponding with the dome apex, and 73 equidistant lines (meridians) radiating out from the center.

3.2. A novel direct method for measuring the thickness at the dome apex

The new theoretical-experimental method proposed by the authors is based on the contactless ultrasonic measurement of the thickness and height of the dome of an elastomer subjected to inflation test. Such a methodology is part of the characterization of materials through the analysis of the acoustoelastic effect [52,57–59]. This effect is given by the variation in ultrasonic longitudinal wave velocity through the sample when the deformation changes, since the state of a solid modified by the strain alters its response to superposed waves.

As known, the measurement of ultrasonic speed requires simultaneous knowledge of the thickness of the material. Several techniques exist in the scientific literature that allow to simultaneously detect both the intrinsic characteristics of the material: the speed, represented by the time of flight (ToF), and the thickness of the sample [60–62].

Fig. 5 shows a schematic drawing of the used method. The dome generated by the elastomeric sample during the bulge test was inflated inside a tank containing water. The dilatation of the dome was constantly detected by an immersion ultrasonic probe positioned along the bulge axis. As shown in Fig. 5, the height of the apex of the dome (h) was derived from the difference between the fixed distance of the transducer from the lower face of the metal clamping flange ($H + \beta$) and the variable distance of the transducer from the apex of the dome (γ). Regarding the description of the times of flight, see section 5.3.

However, whereas an easy pre-calibration for evaluating the longitudinal wave velocity in water is enough to measure the height of the dome, the thickness measurement requires instead the knowledge of the speed in the material as the equibiaxial strain changes. This operation would therefore require the simultaneous measurements of both the ultrasonic wave propagation speed in the material and the equibiaxial deformation undergone by the specimen. Since the conventional techniques adopted for measuring equibiaxial strain (epipolar geometry, DIC or neural network) do not allow operating in water due to refraction phenomena, the ultrasound immersion method cannot be applied simultaneously with the aforementioned techniques.

For this reason, a procedure consisting of the following steps was necessary to be applied:

- Adoption of the stereoscopic reconstruction technique of the SBR-CB20% dome to evaluate the equibiaxial deformation during the bulge test. From the test it was obtained:

$$\varepsilon_{eq} = f(\sigma_{eq}) \tag{17}$$

where f was the experimental function correlating equibiaxial stress (σ_{eq}) and strain (ε_{eq}).

- Simultaneous measurements of both the propagation speed of the ultrasound wave and the thickness in a specimen of the same material subjected to tensile-test (in accordance with the procedure described in Ref. [52]). From the test the following relations were obtained:

$$\varepsilon_{ua} = f'(\sigma_{ua}) \tag{18}$$

and

$$V_L = g(\varepsilon_{ua}) \tag{19}$$

where f' was the experimental function correlating uniaxial stress (σ_{ua}) and strain (ε_{ua}) and g was the function correlating ultrasonic velocity (V_L) and uniaxial strain.

- Under the assumption of congruence between the Von Mises equivalent stresses in uniaxial and equibiaxial state (see Appendix), it was obtained:

$$\varepsilon_{ua} = f''(\varepsilon_{eq}) \tag{20}$$

where f'' was the function correlating uniaxial and equibiaxial strains.

Therefore, from Eqs. (19) and (20):

$$V_L = g'(\varepsilon_{eq}) \tag{21}$$

where g' was the function correlating the ultrasonic speed and the equibiaxial strain. Known the ultrasonic speed in the material, from the measurement of the ToF spent by the wave to cross the specimen, the thickness was obtained.

- Validation of the congruence assumption from the results obtained.

Table 1
Composition of the SBR+20%CB elastomer.

Ingredient	Content (phr)[a]
SBR (1502)	100
CB (N220)	20
ZnO	5
Stearic Acid	2
Antioxidant (TMQ)	1.5
Antiozonant (6PPD)	1.5
Sulfur	5
Accelerator (TBBS)	2

[a] Phr = parts per hundred rubber parts.

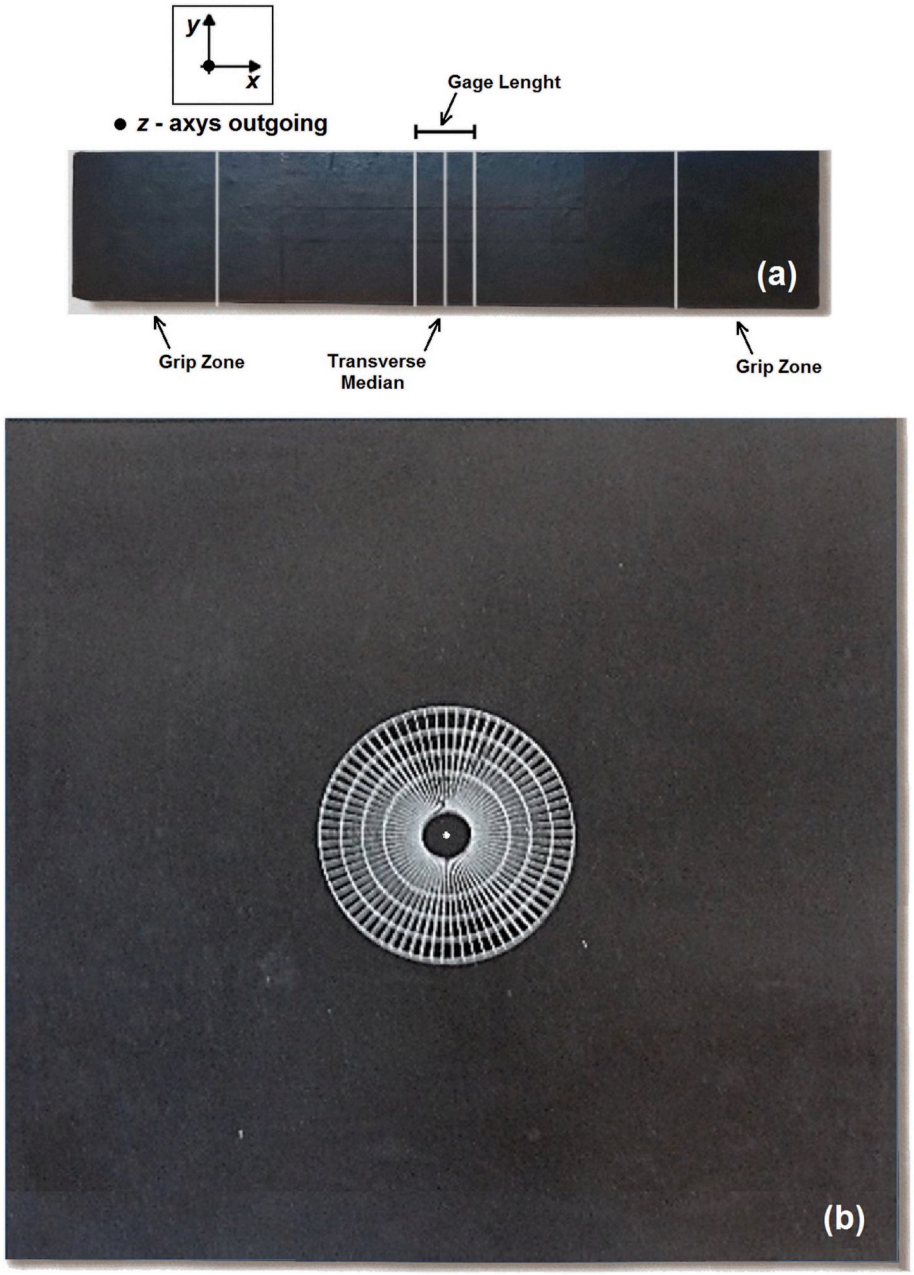

Fig. 4. (a) Uniaxial tensile-test specimen. (b) Bulge test specimen.

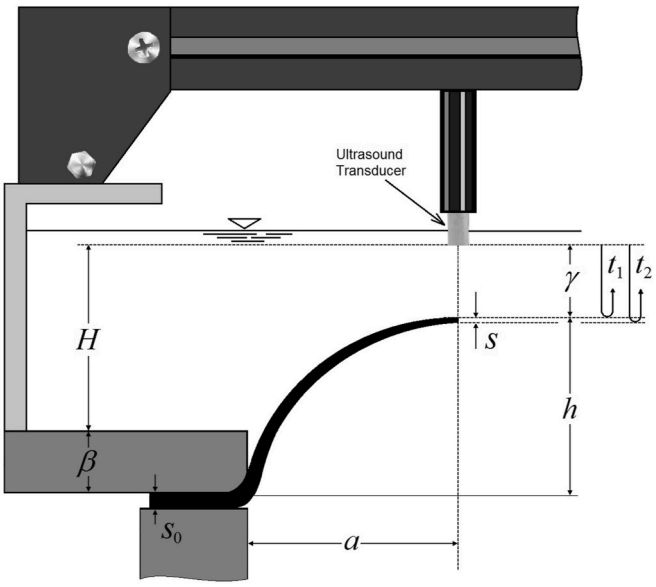

Fig. 5. Schematic drawing of the ultrasound method proposed.

Unlike metal sheets, in elastomeric materials the variation of the longitudinal wave velocity as a function of the strain is not negligible. This justifies the use of the procedure described above, which appears to be more laborious but accurate than previous works focused on the application of ultrasound direct methods to the bulge test [36].

It has also to be noted the slight difference in inflating pressure between the bulge tests performed in air and in water, respectively. This deviation is related to the different specific gravity of fluids that weigh on the dome. Therefore, in order that the two systems can be considered equivalent, the significant parameters of the in-water bulge test should be measured at a pressure p' given by:

$$p' = p + p_{H_2O} = p + \frac{\gamma \cdot p_{atm}}{q_{H_2O}} \tag{22}$$

where p is the in-air bulge pressure, p_{H2O} is the pressure exerted by the water column (γ) along the bulge axis, p_{atm} is the atmospheric pressure and q_{H2O} is the height of the water column exerting the atmospheric pressure.

4. Experimental devices

In this section, the three experimental devices used for the application of the new direct method are outlined. The first two equipments, the testing procedures and the measurement accuracy obtained were described in previous works of the authors [17,40,51,52].

4.1. Setup for immersion ultrasound tensile-test

A schematic drawing of the experimental device able to perform tensile-tests on elastomeric specimens is shown in Fig. 6. This apparatus is equipped with a symmetrical traction system placed on the opposite sides of a water tank, in order to perform the tensile-test on the sample immersed in the coupling fluid. This load symmetry is necessary so that the gage length of the sample always remains within the focal line of the ultrasonic transducer located at the central cross-section of the tank (see

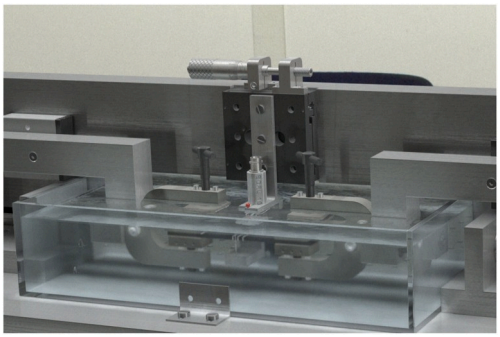

Fig. 7. Detail of the sample immersion condition.

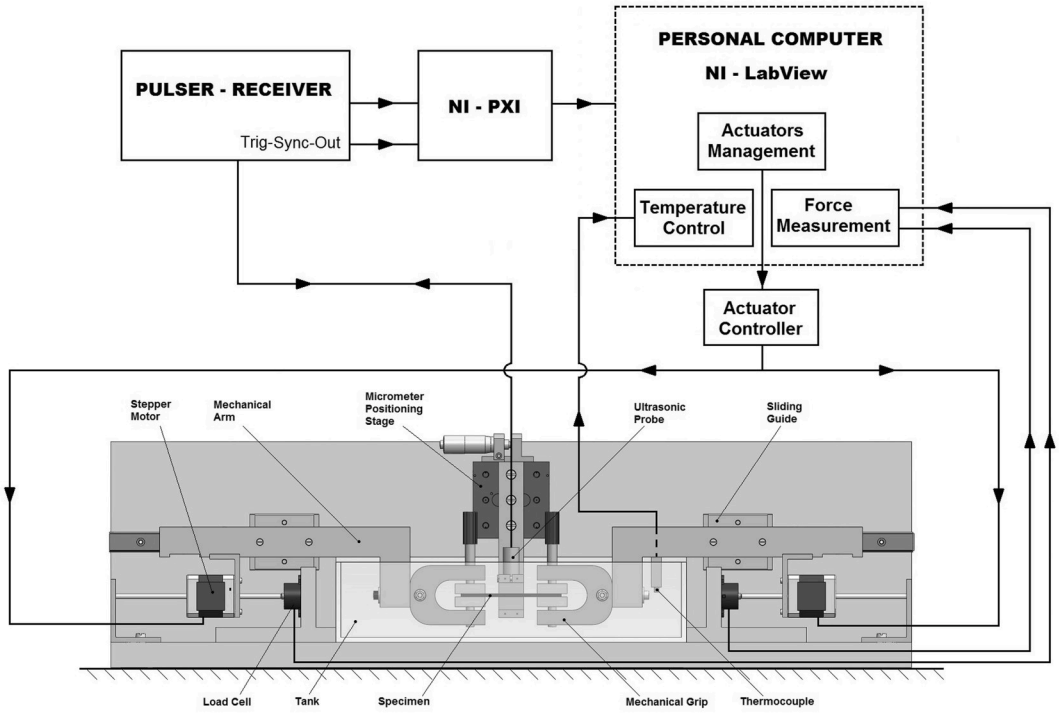

Fig. 6. Schematic drawing of the tensile-testing device [52].

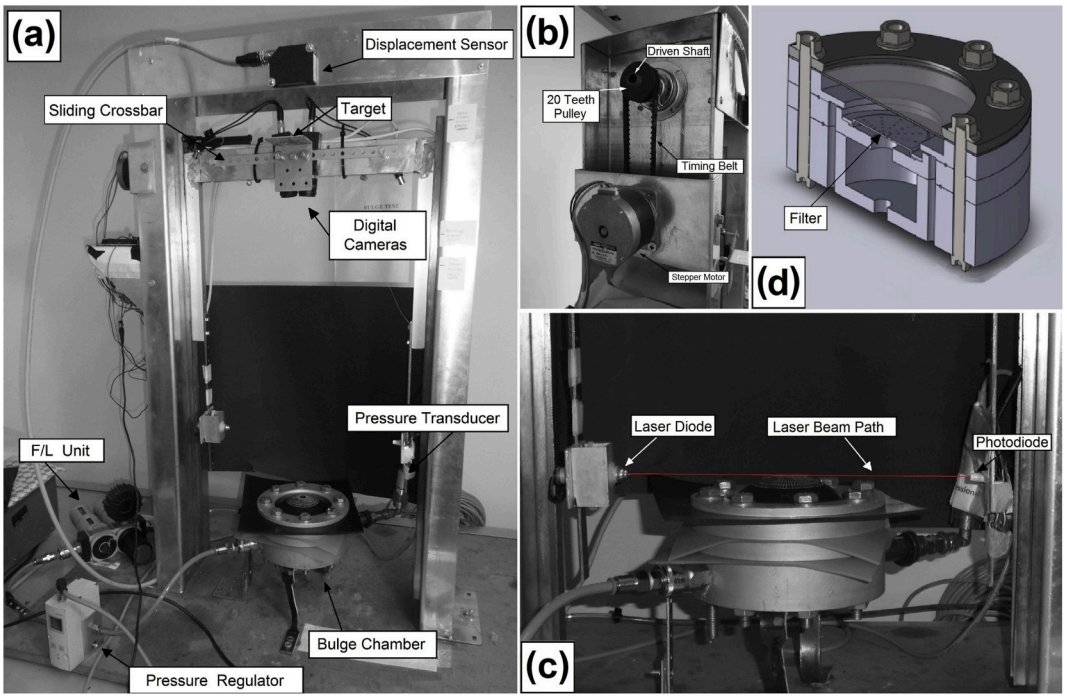

Fig. 8. (a) Overview of the in-air bulge test setup. (b) Detail of the timing belt system. (c) Optical system to regulate the crossbar shifting. (d) Cross-section view of the bulge chamber [17,40].

Fig. 7).

The traction system consists of a pair of grips immersed in the coupling fluid and each placed on the end of an own mechanical arm. Each arm is connected to the casing of a linear actuator having the shaft whose stroke is prevented by a load cell. This causes the double effect of generating a displacement of the casing and the relative arm towards the outside, and of providing the measure of half of the tensile force exerted on the specimen. The sum of the forces measured by the two load cells provides the total tensile force exerted on the sample at any time of the test.

The ultrasonic apparatus consists of a low frequency pulser-receiver (DPR300 - JSR Ultrasonics) conditioning an ultrasound probe (Gilardoni, 2 MHz - BDFL10 Waterproof Line Focused), a NI PXIe-1073 chassis and a host PC. The PXI chassis contains a NI PXI-5114 digitizer module for the capture of the probe output signals (sampling at 125 MHz) and a PXIe-8360 Express Card for high-speed data streaming to the PC. Whole hardware is controlled by NI LabVIEW software. The DPR300 (50 MHz bandwidth) has the double task of generating the compressive waves through the probe and receiving and amplifying (gain = 58 dB) the return echo. The PXIe-5114 digitizes the amplified signal and streams the single A-scan through the PXIe-8360 link to the host.

4.2. In-air bulge test setup

The experimental setup consists of two main elements: a chamber for the bulge test, with a pneumatic inflation system, and a sliding crossbar that supports two cameras for the reconstruction of the dome stereoscopic vision [31,40].

Fig. 8a shows an overview of the in-air bulge test setup. The sliding crossbar is able to shift the two fixed-focus cameras (ImagingSource DMK23G445 monochromatic equipped with FujiFilm HF35HA-1B lens and having a frame rate up to 30 fps) in upward/downward direction in order to follow the inflation and the displacement undergone by the dome apex. In this way, the size of the captured images depends exclusively on the dome deformation and not the distance from lens. The shifting of the crossbar is provided by a timing belt system enable to convert the rotary motion of a stepper motor to a translation of the crossbar via a driven shaft (Fig. 8b). This linear motion is regulated,

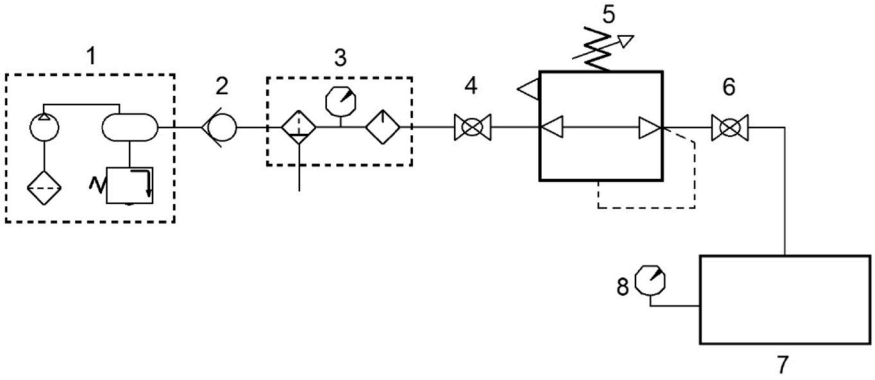

Fig. 9. Pneumatic system scheme: (1) air compressor, (2) non-return valve downstream of the compressor, (3) filtering-lubrication unit, (4) and (6) ball valves, (5) pressure regulator, (7) bulge test chamber, (8) analogic transducer (IFM PA-9024, 0–10 bar) [40].

through a double H-bridge, by an optical system rigidly connected to the crossbar. This optical system, shown in Fig. 8c, consists of an emitter (laser diode) and a photodetector (Hamamatsu Si S5973-01 photodiode) located laterally to the dome. As the laser beam intercepts the inflated dome, the system sends a signal to the motor H-bridge that shifts the crossbar, stopping when the photodiode is newly reached by the laser beam. The H-bridge circuit allows also to invert the verse of the crossbar motion in order to reposition the crossbar at the starting point.

The stepper motor and the drive chain shift the crossbar vertically by 0.125 mm/step, with a 0.03% of focal length error, ensuring a negligible focusing error and enhanced the sharpness of the acquired image. System accuracy matches the size of the captured pixels (37.7 mm). The photodiode diameter is of 0.2 mm, so the laser beam (diameter of 1 mm) does not affect the spatial resolution of the vertical motion (0.2 mm).

To evaluate the uncertainty of the crossbar vertical shifting, a laser triangulation sensor (OptoNCDT 1302–200, with a resolution of 0.2% FSO) was placed on the upper part of the device frame and a target-lamina was fixed to the crossbar (Fig. 8a). Since the measurement provided by the laser sensor is closely related to the height of the dome apex, the bias error of the device will be calculated by comparing the measurement given by the laser with that obtained by the stereoscopic reconstruction.

The compressed air is fed from a hole in the chamber bottom and is uniformly distributed through an intermediate filter. A cross section view of the chamber CAD design is shown in Fig. 8d.

Fig. 9 shows the pneumatic circuit for the air supply.

Particular carefulness was taken for synchronizing, in pseudo real-time, the camera images to data from pressure transducer and displacement sensor. For this purpose, a NI PXIe-1073 chassis containing acquisition boards (PXIe-6341 and PXI-8252), coupled to a PC with dedicated NI LabVIEW software, was used. This software also controls the compressed air supply and regulation system. Additional software (Camera Calibration - MATLAB® Toolbox) was used to calibrate the cameras.

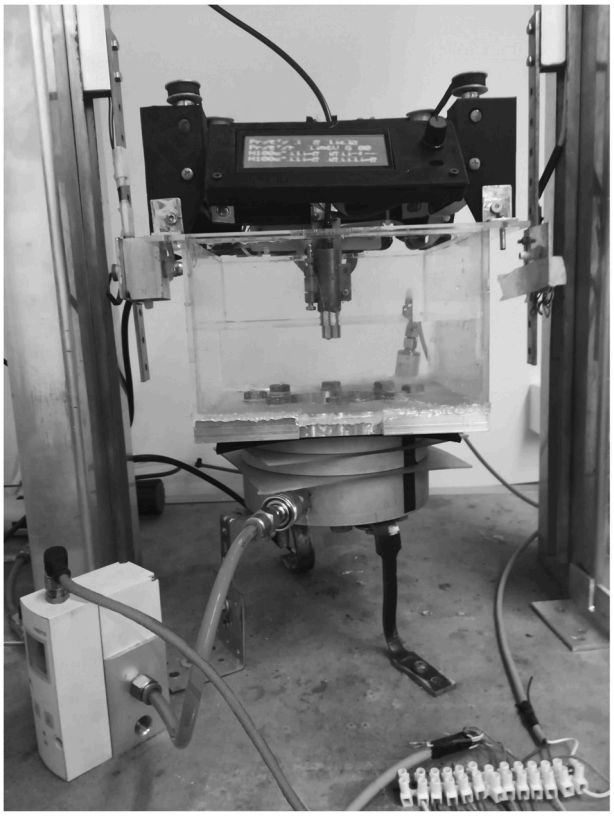

Fig. 10. Overview of the in-water bulge test device.

4.3. In-water bulge test setup

To perform the thickness measurement with ultrasonic immersion technique (pulse-echo) it was necessary to modify the setup described in section 4.2. Stereoscopic reconstruction apparatus, which consists of the sliding crossbar including the cameras and the relative optical system, was replaced by the ultrasonic measurement device. It consists of a tank containing the coupling fluid, above which a *x-y* positioning system for the immersion ultrasonic transducer was fixed.

The tank has Plexiglas sidewalls of 4 mm thickness and an aluminum base, suitably shaped and drilled, which replaces the upper flange of the bulge chamber. The whole in-water bulge test device is shown in Fig. 10.

The positioning system (Computer Numerical Control, CNC) allows the ultrasound probe, inserted in a vertical position inside a support, to move on a plane parallel to the undeformed specimen. This movement, obtained from the set of three stepper motors (Nema17) with relative timing belt connections (GT2) and managed by a microcontroller board (Arduino mega 2560), can be controlled directly by a smart control display or by PC using the software Repetier-Host.

The ultrasonic apparatus is the same of that used in section 4.1. The only difference with the system used in the uniaxial test is the ultrasonic probe type. In this case, the line-focused probe was replaced with a spot-focused probe (Gilardoni, 2 MHz - BDFP10 Waterproof Spot Focused) to reduce the area affected by the ultrasound beam to a neighborhood of the dome apex, thus increasing the measurement accuracy.

5. Experimental tests and results

5.1. Ultrasonic uniaxial test

Ten rectangular-shaped specimens, obtained from the same sheet and having the characteristics described in section 3.1, were tested.

As mentioned in section 4 about the test execution mode, reference was made to a previous work of the authors [52]. Measurements were performed through immersion ultrasonic pulse-echo technique, in order to simultaneously obtain times of flight and sample thickness according to the method of Hsu et al. [61]. Results achieved are reported in Table 2 with notations of Fig. 11. This figure shows the support holding the ultrasonic probe, designed in agreement with the above method [61].

It has to remember that the test procedure requires a preliminary measurement of the ToF without the specimen (t_w), as shown in Fig. 11, in order to determine the velocity of the longitudinal wave (V_w) in the medium used (distilled water at 20 °C), being known the distance between transducer and reflector ($D = 29$ mm). The mean value of longitudinal wave was $V_w = 1481.9 \pm 2.2$ m/s, in good accordance with the value found in scientific literature [63].

Since D is the only well-known length, it was chosen as the reference for quality control of measurements performed by the experimental setup. The mean value ($\overline{D}$) obtained is:

$$\overline{D} = 28.96 \pm 0.08 \text{ mm}$$

The percentage error on the measure of D is:

$$\frac{\Delta D}{D} = \left|\frac{\overline{D} - D}{D}\right| * 100 = 0.15\% \tag{23}$$

The value obtained from (23) is an indication of the high accuracy of the whole ultrasonic tensile-test device.

Fig. 12 shows an example of NI-LabView front panel at 5% strain. The figure shows an overall ultrasonic A-Scan, the first echo and the cross-correlation curve for t_1 signal, respectively. As known, the analysis of the signal echo cross-correlation function allows evaluating the time delay between the 1st and 2nd echo to determine accurately the ToFs [52].

Table 2
Significant geometrical parameters of the ultrasonic tensile test as the strain changes.

Strain	t_1	t_2	t_s	D_1	D_2	s	D	V_L
%	[μs]	[μs]	[μs]	[mm]	[mm]	[mm]	[mm]	[m/s]
0	18.10	21.00	37.82	13.41	12.46	3.02	28.89	2082.3
5	18.13	21.06	37.90	13.43	12.48	2.95	28.86	2012.9
10	18.17	21.07	38.05	13.46	12.58	2.87	28.91	1974.4
15	18.23	21.09	38.24	13.51	12.71	2.80	29.02	1961.7
20	18.31	21.10	38.30	13.57	12.74	2.72	29.03	1951.6
25	18.35	21.08	38.32	13.60	12.77	2.65	29.02	1943.8
30	18.42	21.09	38.38	13.65	12.81	2.58	29.04	1934.9
35	18,49	21.08	38.21	13.70	12.69	2.50	28.89	1930.0

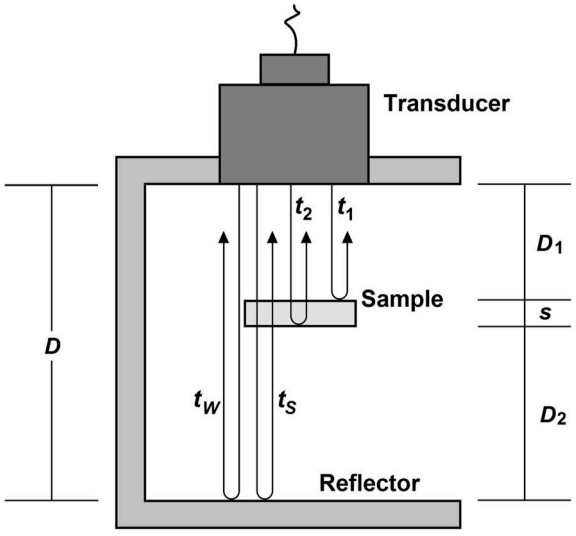

Fig. 11. Measurement configuration for immersion ultrasonic technique [52].

Table 3 shown the mean results (N = 10 samples) obtained in order to characterize uniaxially the isotropic SBR+20%CB material.

From the measured values of the thickness (s), the strain along the z-direction (ε_z) (see Cartesian coordinate system in Fig. 4) was obtained and then, known the strain along x-axis (ε_x), the Poisson ratio ν. The mean value found ($\bar{\nu}$= 0.493) was in agreement with the results of a previous work of the authors on SBR+20%CB material [51].

The strain along the y-direction (ε_y) was equal to the ε_z due to the isotropy of the material tested.

The 5th column shows the values of the sample width (b) calculated from the knowledge of ε_y.

Finally, in 6th and 7th columns the tensile-force (F) and the stress (σ_{ua}) values corresponding to the deformations imposed are indicated, respectively.

From the results obtained, Eqs. (18) and (19) become respectively:

$$\varepsilon_{ua} = 0.0356\ \sigma_{ua}^2 + 0.0703\ \ \sigma_{ua} + 0.0047 \tag{24}$$

$$V_L = 53156\ \ \varepsilon_{ua}^4 - 45222\ \ \varepsilon_{ua}^3 + 14148\ \ \varepsilon_{ua}^2 - 2114.8\ \ \varepsilon_{ua} + 2082.3 \tag{25}$$

5.2. In-air bulge test

The maximum pressure in the bulge chamber was fixed at 100 kPa, slightly lower than the limit value of the specimen burst, which was determined during calibration procedure.

The two cameras were stereoscopically calibrated through *Camera Calibration's Toolbox,* which adopts 3D target calibration on the pinhole model [64]. By acquiring images of a flat grid (15 mm × 15 mm with 1 mm b&w squares) variously oriented to the cameras, the three intrinsic parameters (focal length, image center and distorsion factors) and the two extrinsic factors (rotation and translation vectors) were obtained [17]. These factors, shown in Table 4, define the relative position between right and left camera.

Cameras separation not more than 10% of working distance (u) ensures the entire grid is acquired. Therefore, at a distance of 40 mm between the two cameras, the distance from the sample at 400 mm was set. Furthermore, a focal length of 10,550 px and a minimum focusing range from 250 mm to ∞ were set.

The program, developed in NI-LabVIEW, acquires under request the inflating pressure and crossbar displacement data from the machine and a single frame of the specimen at a given instant. In order to make more accurate the measure, the system acquires 33 samples at a sample rate of 1 kHz for each image. Under these conditions, the time required for each acquisition was of 1/30 s, corresponding to the frame rate of cameras. Therefore, the software acquires the frame and, between each acquisition and the next one, calculates the average of the 33 values, which takes as best value, and determines the standard deviation of the series. Thus, the synchronization error was reduced to 1/30 s, corresponding to the phase shift of a single frame.

To improve the sharpness, each image was subjected to some preprocessing stages: first, the image was converted to grayscale (Fig. 13a), and then filtered with the convolution (Fig. 13b) and median filters (Fig. 13c).

Fig. 14 shows the 3D reconstruction process, based on epipolar geometry. The epipolar geometry of acquired images in a stereoscopic system provides a strong constraint at the corresponding points in two images of the same scene. In the reference system fixed the origin coincides with the center of the clamping flange, the vertical z-axis passes through the midpoint between the focal centers of the two cameras, the x-axis is oriented to the right of the testing machine on the median plane and the y-axis is perpendicular to x and z. The sample was oriented so that the first meridian was along the x-axis. The 73 meridians were numbered anticlockwise starting from the first one.

Dome 3D reconstruction was obtained using markers shown in Fig. 15 [17]. The markers, highlighted through the edge-detection filter, are transition points between light and dark areas of the image and correspond, in the case in question, to the intersections between the 73 meridians and the 5 parallels of the screen-printed grid on the specimen (Fig. 15a). Fig. 15b highlights the homothetic markers selected in the reconstruction of the grid.

Fig. 16 shows an example of the dome stereoscopic reconstruction obtained.

Once the inner radius of the bulge chamber was fixed (a = 50 mm), Table 5 shows the mean values obtained by testing five specimens as the inflating pressure changes. Values of the dome height (h) correspond to the difference between 3D coordinates of the top and the base of the dome at each inflating pressure. The measurement of the equibiaxial strain (ε_{eq}), according to Eq. (2), was obtained by comparing the distances between two successive homothetic markers relating to two different pressure conditions. An example of this comparison is shown in Fig. 15c. The radius of the dome (R) is obtained from Eq. (6).

As a first approximation, considering an elastic-linear behavior of the material, the thickness value as a function of the strain along the z-axis

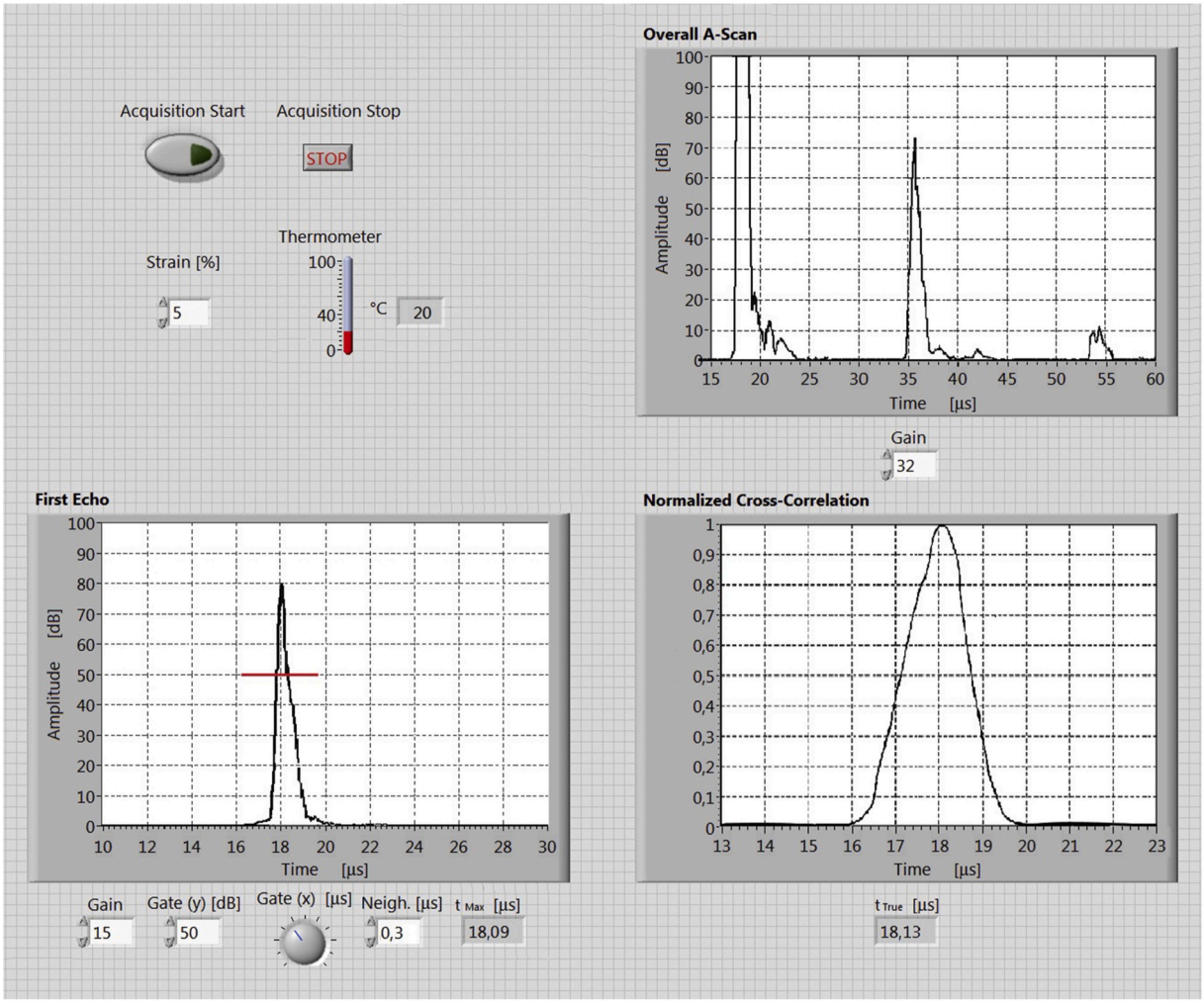

Fig. 12. Front panel of the NI LabView software at 5% strain.

Table 3
Significant mechanical parameters of the ultrasonic tensile test as the strain changes.

$\varepsilon_x = \varepsilon_{ua}$	s	$\varepsilon_z = \varepsilon_y$	ν	b	F	σ_{ua}
–	[mm]	–	–	[mm]	[N]	[MPa]
0	3.02	0	–	25.00	0.00	0.00
0.05	2.95	−0.025	0.493	24.38	30.49	0.42
0.10	2.87	−0.049	0.495	23.76	55.81	0.81
0.15	2.80	−0.074	0.493	23.15	76.57	1.18
0.20	2.72	−0.099	0.496	22.52	92.20	1.49
0.25	2.65	−0.124	0.494	21.91	102.24	1.73
0.30	2.58	−0.147	0.489	21.33	108.37	1.94
0.35	2.50	−0.172	0.492	20.69	110.00	2.08
			$\bar{\nu}$ = **0.493**			

Table 4
Optimized stereoscopic calibration parameters.

Intrinsic Parameters	Left Camera	Right Camera
Focal Length [px]	[10541.62 ÷ 10647.18]	[10471.16 ÷ 10569.41]
Image center [px]	[1304.47 ÷ 651.12]	[1720.13 ÷ 884.19]
Distorsion Factors	[1.34–57.67 0.02 0.017 0.00]	[0.38–21.24 0.014 0.008 0.00]
Extrinsic Factors	**Value**	
Rotation Vector	[0.04218–0.14268 -0.01103]	
Translation Vector	[45.24871–0.03476 2.31881]	

was calculated by applying Eq. (7):

$$s = s_0 e^{-\varepsilon_z} \tag{26}$$

where, according to Eq. (3), $\varepsilon_z = \varepsilon_3 = -2\varepsilon_1 = -2\varepsilon_{eq}$.

From the Boyle-Mariotte law expressed by Eq. (1), the value of the equibiaxial stress was finally obtained as the strain changes.

From the results obtained Eq. (17) becomes:

$$\varepsilon_{eq} = 0.0491 \;\; \sigma_{eq}^2 + 0.1199\, \sigma_{eq} - 0.0029 \tag{27}$$

Then, the congruence between uniaxial and equibiaxial equivalent stresses according to Von Mises, demonstrated in the Appendix, allowed to obtain the following experimental form for Eq. (20):

$$\varepsilon_{ua} = 6.7143 \;\; \varepsilon_{eq}^3 - 2.4239 \;\; \varepsilon_{eq}^2 + 0.8806 \;\; \varepsilon_{eq} - 0.0021 \tag{28}$$

Therefore, from Eqs. (25) and (28):

$$V_L = -10920\, \varepsilon_{eq}^3 + 6538 \;\; \varepsilon_{eq}^2 - 1468 \;\; \varepsilon_{eq} + 2082.3 \tag{29}$$

As a confirmation of the congruence assumption from which Eq. (29) derives, the curves V_L-σ_{ua} and V_L-σ_{eq} fit well each other as shown in Fig. 17. Indeed, the authors have analytically determined that the point of maximum deviation between the curves V_L-σ_{ua} and V_L-σ_{eq} occurs for σ = 0.75 MPa and is equal to 7.29 m/s. This corresponds to a percentage error of 0.37% and is proof of agreement between the curves.

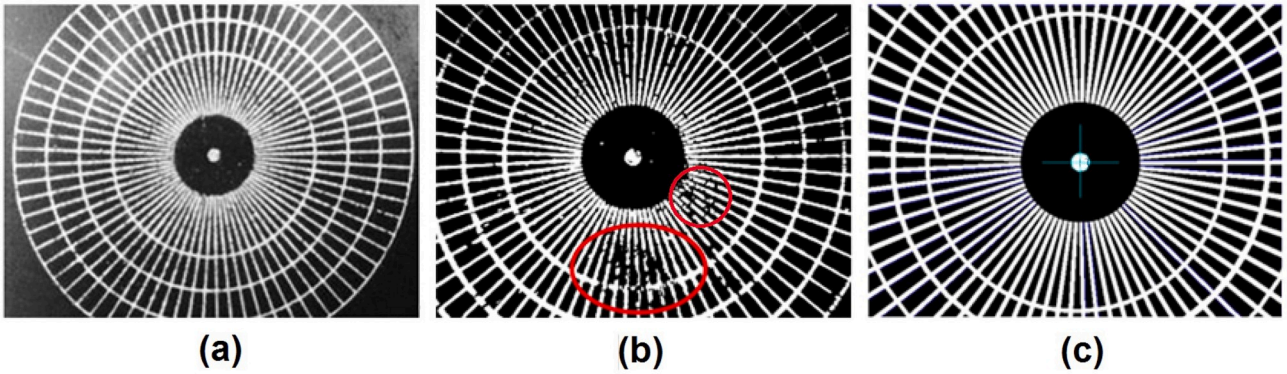

Fig. 13. Image pre-processing stages. (a) Grayscale image. (b) Convolution-filtered image. (c) Median-filtered image to recover the attenuated-light areas as red encircled in (b). . (For interpretation of the references to colour in this figure legend, the reader is referred to the Web version of this article.)

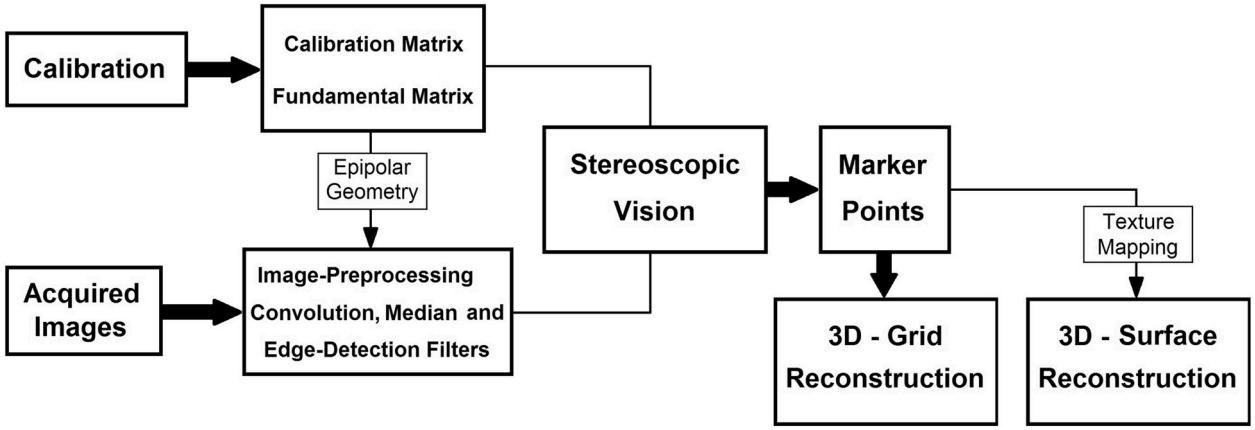

Fig. 14. 3D reconstruction process [17,40].

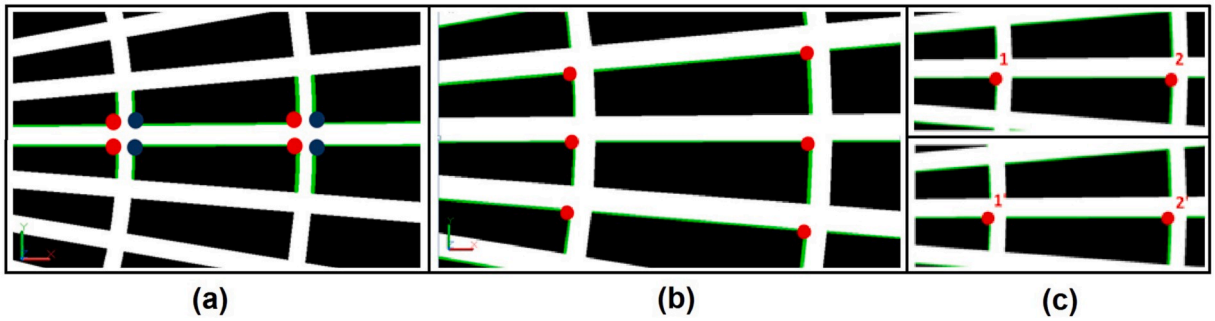

Fig. 15. (a) Light transitions: dark to light (red point) and light to dark (blue point). (b) Homothetic markers. (c) Comparison of the distance between two homothetic markers at two successive stress states [17]. (For interpretation of the references to colour in this figure legend, the reader is referred to the Web version of this article.)

5.2.1. Analysis of the bias error on the measurement of the dome apex height

With notations of Fig. 18, from the laser measurement (e), known both the distance ($m = 75$ mm) between the target-lamina and the lens plane of the two cameras, and the distance ($v = 680$ mm) between the displacement laser sensor and the base of the upper flange of the bulge chamber, being the working distance ($u = 400$ mm) between lens plane and the dome apex set in section 5.2, the indirect measurement of the height of the dome apex (h_{laser}) is given by:

$$h_{laser} = v - m - u - e \tag{30}$$

To evaluate the bias uncertainty of the stereoscopic technique, the h_{laser} value at each pressure step was considered as reference standard measurement.

Table 6 shows the comparison between the mean values of the apex height from the displacement sensor and from the 3D reconstruction ($h_{stereoscopic}$) as the inflating pressure changes. The mean bias error (MBE) was:

$$MBE = \frac{1}{sn}\sum_{i=1}^{sn}\left(h_{laser,\,i} - h_{stereoscopic,i}\right) = 0.21 \text{ mm} \tag{31}$$

where $sn = 19$ is the number of pressure steps.

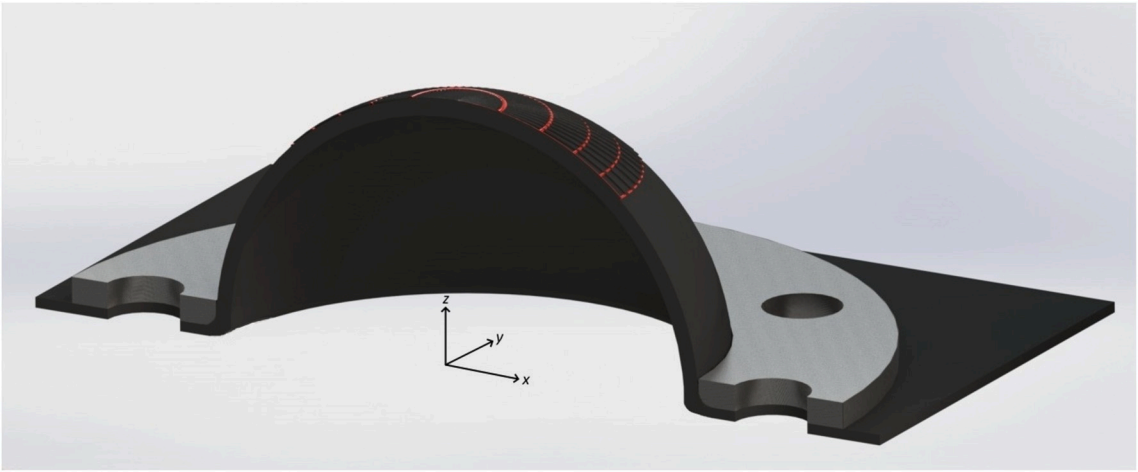

Fig. 16. 3D reconstruction of the dome.

Table 5
Main parameters of the in-air bulge test.

p	h	ε_{eq}	R	s	σ_{eq}
[MPa]	[mm]	–	[mm]	[mm]	[MPa]
0	0	0	∞	3.02	0
0.015	13.62	0.026	98.60	2.87	0.26
0.020	13.99	0.036	96.37	2.81	0.34
0.025	14.88	0.046	91.44	2.76	0.41
0.030	15.84	0.056	86.82	2.70	0.48
0.035	16.87	0.067	82.52	2.64	0.55
0.040	17.98	0.078	78.53	2.58	0.61
0.045	18.94	0.093	75.47	2.51	0.68
0.050	20.40	0.102	71.47	2.46	0.73
0.055	21.72	0.115	68.41	2.40	0.78
0.060	23.10	0.128	65.66	2.34	0.84
0.065	24.53	0.142	63.22	2.27	0.90
0.070	25.99	0.156	61.09	2.21	0.97
0.075	27.44	0.171	59.27	2.14	1.04
0.080	28.84	0.187	57.76	2.08	1.11
0.085	29.91	0.224	56.75	1.93	1.25
0.090	31.18	0.236	55.68	1.89	1.33
0.095	31.94	0.265	55.10	1.78	1.47
0.100	32.32	0.283	54.84	1.71	1.60

5.3. In-water bulge test

Testing procedure involves an initial check on the tightening of the bolts of the upper flange (base of the tank). If this tightening is carried out correctly, the center of the circumference screen-printed on the undeformed specimen will coincide with the dome apex under a deformed state. This check is performed by means of a laser pointer housed in the ultrasonic probe support and positioned, through the CNC system, at the geometric center of the upper flange hole. The laser spot must coincide with the center screen-printed for the duration of the check bulging (Fig. 19).

Once the laser pointer was replaced with the immersion ultrasonic probe, the second step of the test, as in section 5.1, involved the measurement of the ultrasonic wave speed (Vw) in the coupling fluid (distilled water at $T = 25$ °C) being known the distance ($H = 44.75$ mm) between transducer and tank aluminum base (Fig. 5). The same specimens as in section 5.2 were tested and the mean value of the longitudinal wave velocity was $V_w = 1497.2 \pm 2.2$ m/s, in good accordance with the value found in scientific literature [63].

Using hardware and software described in section 5.1, with notations of Fig. 5, the quantities reported in Table 7 were measured.

The second column of Table 7 shows the pressure values (p') calculated by Eq. (22) taking into account the water column on the dome. However, the extremely small deviation between the values p' and p (relative to the bulge test in air) makes the use of the former ones superfluous.

With reference to Fig. 5, in Table 7 the values of the measured ToFs are reported:

- t_1 = ToF between ultrasound probe and upper surface of the dome;
- t_2 = ToF between ultrasound probe and lower surface of the dome.

The specimen crossing time (t_s) was derived from the difference between t_2 and t_1.

The distance γ was obtained from the product of $t1$ and the previously measured ultrasonic velocity in water (Vw). As stated in section 3.2, the height of dome apex ($h_{ultrasonic}$) was derived from the knowledge of quantities H, β and γ, as well as dome radius values (R) were calculated by Eq. (6).

To calculate the thickness at the dome apex (s) as a function of the inflating pressure, the respective V_L values, obtained applying Eq. (29), were used:

$$s = V_L \cdot t_s \tag{32}$$

Finally, equibiaxial stress values (σ_{eq}) were calculated by Eq. (1).

Table 8 shows the dome apex height found via ultrasonic (Table 7) and stereoscopic (Table 6) techniques, respectively, when the inflating pressure changes. Table 8 shows also the percentage error calculated by assuming $h_{stereoscopic}$ as reference standard measurement.

The very low value of the mean percentage error found ($\bar{e} = 0.26\%$) was a further confirmation of the validity of the assumption made and the device accuracy.

6. Analysis of results

Fig. 20 is a review of curves of the thickness at the dome apex obtained, as the height of the dome changes, by applying both the main theoretical models listed in section 2.2 and the two measurement techniques proposed in this paper. First technique was a 3D reconstruction of the dome exploiting the elastic-linear theory expressed in Eq. (26) and the second technique was a contactless ultrasonic measurement of the thickness and height at the dome apex.

It has to be noted that the curve deriving from 3D reconstruction falls within the limit curves from Jovane [21] and Hill-Marciniak [20,46] models and fits well with the curve from Charalambides model [44], formulated for soft materials. However, the trend of the curve from ultrasonic technique seems to better reflect the viscoelasticity of the material that results in a greater decrease in thickness as the pressure and, consequentially, the height increase.

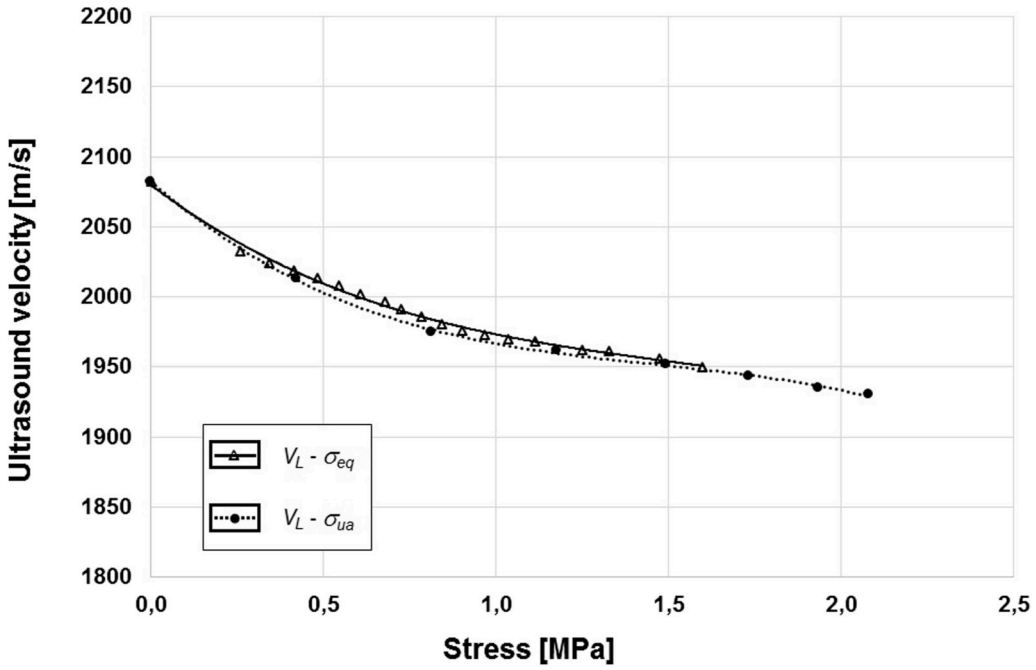

Fig. 17. Ultrasound wave velocity as equibiaxial and uniaxial stresses change.

The equation that best describes the trend of thickness as a function of height, obtained with the ultrasonic technique, is:

$$s = s_0 - \frac{kh^3}{a^2} exp^{-\frac{2h^2}{3a^2}} \tag{33}$$

where $k = 0.130$ is a dimensionless constant.

6.1. Proposal of a new theoretical-experimental model for elastomers

As known, the hyperelastic behavior of rubber-like materials was expressed through the strain energy density function (W) introduced for the first time by Mooney and Rivlin [1,2]:

$$W = C_1(I_1 - 3) + C_2(I_2 - 3) \tag{34}$$

where C_1 and C_2 are material constants, and I_1 and I_2 represent the first and second invariant of Cauchy-Green tensor, respectively.

However, they did not take the small compressibility of the materials into account. The introduction of the third invariant of the Cauchy-Green tensor (I_3) allowed considering the effective material compressibility within the W function [50]:

$$W = C_1(I_1 - 3) + C_2(I_2 - 3) + (C_1 + C_3)(I_3 - 1) + 2(- 2C_1 - 2C_2 - C_3)\left(\sqrt{I_3} - 1\right) + C_4\left(\sqrt{I_3} - 1\right)^3 \tag{35}$$

where C_3 and C_4 are higher-order material constants.

It is known that the constants C depend on the Lamé constants (μ e λ) of the material [51], and in particular:

$$C_1 + C_2 = \frac{\mu}{2} = \frac{G}{2} = \frac{E}{4(1+\nu)} \tag{36}$$

$$C_3 = \frac{\lambda}{2} = \frac{\nu \cdot E}{2(1+\nu)(1-2\nu)} \tag{37}$$

where G and E are the shear modulus and elastic modulus, respectively.

With reference to experimental data from the uniaxial tensile test, shown in Table 3, the mechanical characteristics of the SBR+20%CB analyzed were: $E = 10.9$ MPa, $G = 3.65$ MPa, $\nu = 0.493$. Therefore, the values of the constants will be: $C_1 + C_2 = 1.825$ MPa and $C_3 = 128.545$ MPa.

The authors propose a review of Eq. (33) based on the volume change of the tested elastomer, taking C material constants into account. Particularly, the dimensionless constant k becomes:

$$k = 9\left(\frac{C_1 + C_2}{C_3}\right) \tag{38}$$

From Eqs. (36) and (37):

$$k = 4.5\left(\frac{1-2\nu}{\nu}\right) = 0.128 \tag{39}$$

and then:

$$s = s_0 - 4.5\frac{(1-2\nu)h^3}{\nu \cdot a^2} exp^{-\frac{2h^2}{3a^2}} \tag{40}$$

As shown in Fig. 21, the curve of the thickness at the dome apex deriving from this approach matches with that from ultrasonic method.

Therefore, the model expressed by (40) represents a general equation to define the thickness of the dome generated by SBR+20%CB subjected to a bulge test.

7. Discussion

To evaluate the discrepancy level between the theoretical and the experimental model (Fig. 21), respectively expressed by eqs. (40) and (33), uncertainty under the most severe working condition was considered. This condition occurs at the maximum value of the standard deviations ($St.dev_{max} = 0.05$ mm) calculated with respect to the relative best values of the dome height h_{best} for each inflating pressure p. As stated in 5.2 and 5.3 sections, the best values were calculated for the set of 5 tested specimens. The uncertainty on the thickness measurement for

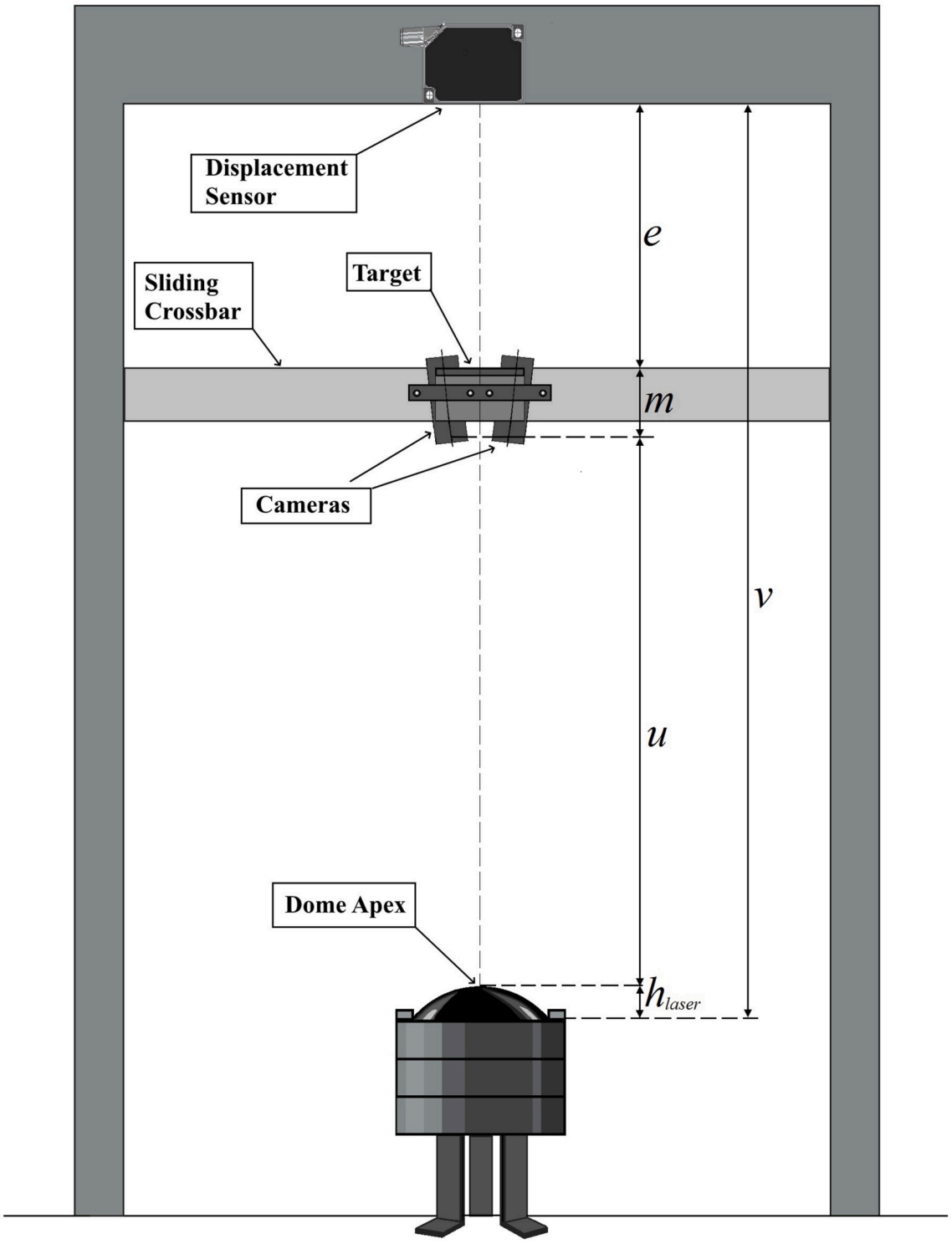

Fig. 18. Geometrical configuration of the laser sensor measurement.

Table 6
Comparison between height values from laser sensor and 3D reconstruction.

p[MPa]	h_{laser}[mm]	$h_{stereoscopic}$[mm]	$h_{laser} - h_{stereoscopic}$[mm]
0.000	0.00	0.00	0.00
0.015	13.79	13.62	0.17
0.020	14.20	13.99	0.21
0.025	15.06	14.88	0.18
0.030	16.02	15.84	0.18
0.035	17.05	16.87	0.18
0.040	18.22	17.98	0.24
0.045	19.16	18.94	0.22
0.050	20.63	20.40	0.23
0.055	21.91	21.72	0.19
0.060	23.30	23.10	0.20
0.065	24.76	24.53	0.23
0.070	26.24	25.99	0.25
0.075	27.70	27.44	0.26
0.080	29.10	28.84	0.26
0.085	30.20	29.91	0.29
0.090	31.40	31.18	0.22
0.095	32.20	31.94	0.26
0.100	32.53	32.32	0.21
			***MBE* = 0.21**

Fig. 19. Laser check of the bolts tightening.

Table 8
Percentage error on the measurements of the height at the dome apex.

p	$h_{ultrasonic}$	$h_{stereoscopic}$	Error
[MPa]	[mm]	[mm]	%
0.000	0.00	0.00	–
0.015	13.70	13.62	0.63
0.020	14.05	13.99	0.44
0.025	14.92	14.88	0.23
0.030	15.90	15.84	0.39
0.035	16.94	16.87	0.38
0.040	18.06	17.98	0.47
0.045	18.96	18.94	0.10
0.050	20.47	20.40	0.33
0.055	21.77	21.72	0.24
0.060	23.11	23.10	0.01
0.065	24.54	24.53	0.04
0.070	26.05	25.99	0.24
0.075	27.48	27.44	0.12
0.080	28.90	28.84	0.20
0.085	29.95	29.91	0.12
0.090	31.28	31.18	0.31
0.095	32.01	31.94	0.22
0.100	32.37	32.32	0.17
			$\bar{e}$ = 0.26%

both models derives from that calculated on the h_{best} measurement.

In columns 5 and 6 of Table 9 are reported respectively the maximum and minimum values of h derived from the adoption of $St.dev_{max}$ as uncertainty at each inflating condition. From eq. (33), the extreme values of the error range on the experimental measurement of the thickness (7th and 8th column) were obtained at each inflating condition. Similarly, from eq. (40) the extreme values of the error range on the theoretical estimation of the thickness (9th and 10th column) were found.

Column 11 shows the maximum deviation between the two curves at each h_{best} value, given by the difference between the maximum value of the error range of one curve and the minimum value of the error range of the other curve ($Deviation\ max = s_{theor,max} - s_{exp,min}$).

Last column shows the percentage error taking the experimental approach as a reference. The maximum percentage error value found was 1.85%.

Table 7
Main parameters of the in-water bulge test.

	p' [MPa]	p [MPa]	t_1 [μs]	t_2 [μs]	t_s [μs]	γ [mm]	$h_{ultrasonic}$ [mm]	R [mm]	V_L [m/s]	s [mm]	σ_{eq} [MPa]
a = 50 mm	0.000	0.00	41.91	43.36	1.45	62.75	0.00	∞	2082.3	3.02	0.00
H = 44.75 *mm*	0.0155	0.015	32.76	34.21	1.45	49.05	13.70	98.07	2032.7	2.94	0.25
	0.0205	0.020	32.53	33.97	1.44	48.70	14.05	96.01	2024.1	2.90	0.33
β =18 mm	0.0255	0.025	31.95	33.37	1.42	47.83	14.92	91.26	2019.0	2.86	0.40
T = 25 °C	0.0305	0.030	31.29	32.69	1.40	46.85	15.90	86.55	2013.6	2.82	0.46
	0.0354	0.035	30.60	31.98	1.38	45.81	16.94	82.27	2008.0	2.77	0.52
V_W =1497.2 m/s	0.0404	0.040	29.85	31.20	1.35	44.69	18.06	78.24	2002.3	2.71	0.58
T [°C]	0.0454	0.045	29.25	30.58	1.33	43.79	18.96	75.41	1996.7	2.65	0.64
	0.0504	0.050	28.24	29.54	1.30	42.28	20.47	71.30	1990.9	2.58	0.69
	0.0554	0.055	27.37	28.64	1.27	40.98	21.77	68.30	1985.6	2.51	0.75
	0.0604	0.060	26.48	27.71	1.23	39.64	23.11	65.65	1980.6	2.44	0.81
	0.0654	0.065	25.52	26.71	1.19	38.21	24.54	63.20	1976.3	2.35	0.87
	0.0704	0.070	24.51	25.66	1.15	36.70	26.05	61.00	1972.7	2.27	0.94
	0.0753	0.075	23.56	24.67	1.11	35.27	27.48	59.23	1970.0	2.18	1.02
	0.0803	0.080	22.61	23.67	1.06	33.85	28.90	57.70	1968.4	2.08	1.11
	0.0853	0.085	21.91	22.92	1.01	32.80	29.95	56.71	1962.2	1.98	1.22
	0.0903	0.090	21.02	21.97	0.95	31.47	31.28	55.60	1961.5	1.88	1.33
	0.0953	0.095	20.53	21.43	0.90	30.74	32.01	55.05	1955.9	1.76	1.48
	0.1003	0.100	20.29	21.13	0.84	30.38	32.37	54.80	1950.0	1.65	1.66

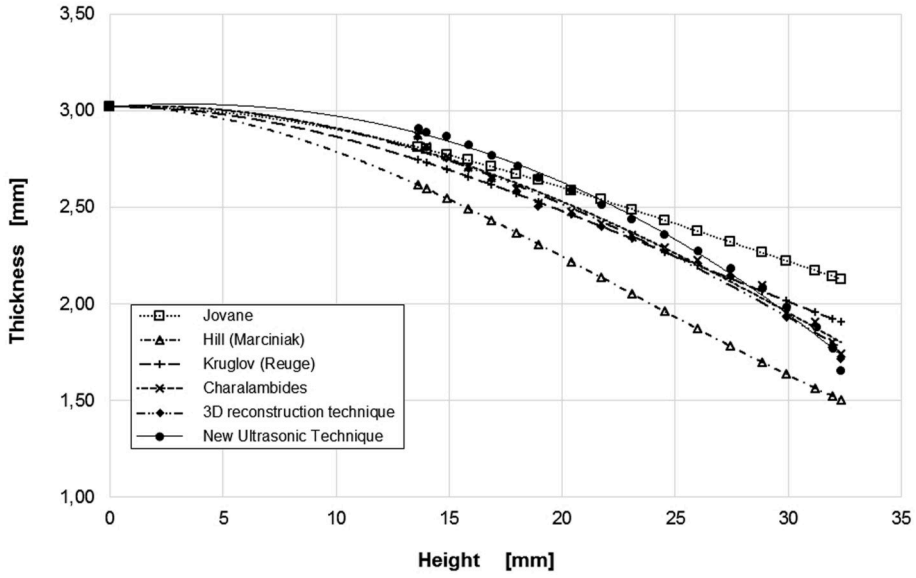

Fig. 20. A review of the curves of the dome thickness as a function of the height, obtained from different analytical models.

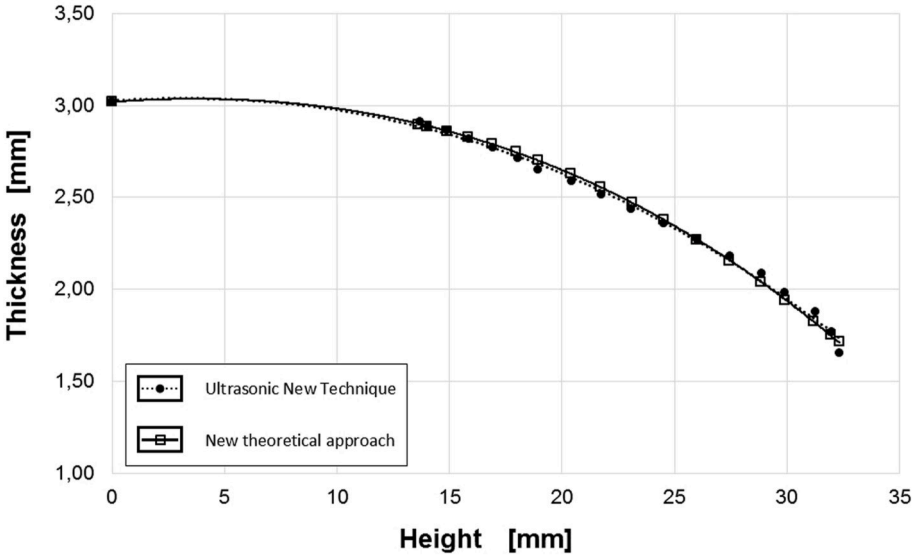

Fig. 21. Comparison between thickness curves deriving from the new ultrasonic technique and from the new theoretical approach.

8. Conclusion

A first element of novelty in this paper is the intuition of the authors to determine a function correlating uniaxial strains from tensile test to equibiaxial strains from bulge test through the assumption of congruence between the equivalent stresses of Von Mises in uniaxial and equibiaxial state. From this function is derived a helpful relation linking the ultrasonic wave velocity to the equibiaxial strain.

A second innovation consists in suggesting a theoretical-experimental method based on the contactless ultrasonic measurement of both the thickness and height at the apex of the dome in bulge-tested elastomeric samples. Such a methodology allows mechanically characterizing rubber-like materials via the investigation of the acoustoelastic effect.

A further novelty is represented by the proposal of a theoretical-experimental model to estimate the dome thickness, suitable for elastomers and alternative to the analytical approaches in the scientific literature. This model is able to take the slight material compressibility into account through knowledge of the Poisson ratio only. It has to be noted as all of the thickness values obtained when the height of the dome apex changes falls within a percentage error range of 1.85%, assuming the corresponding values obtained via the new ultrasonic technique as reference standard values.

The greatest discrepancy between the theoretical and the experimental curve was found at the highest values of the height of the dome and this can be depend on the initial assumption of “small deformations”

Table 9
Discrepancy parameters between experimental and theoretical model.

p	h_{best}	s_{exp}	s_{theor}	h_{max}	h_{min}	$s_{exp,min}$	$s_{exp,max}$	$s_{theor,min}$	$s_{theor,max}$	Deviation max	Error
[MPa]	[mm]	[mm]	[mm]	[mm]	[mm]	[mm]	[mm]	[mm]	[mm]	[mm]	%
0.0155	13,70	2,91	2,90	13,75	13,65	2891	2894	2893	2896	0,005	0,16
0.0205	14,05	2,88	2,89	14,10	14,00	2882	2885	2884	2887	0,005	0,17
0.0255	14,92	2,86	2,86	14,97	14,87	2856	2859	2858	2861	0,006	0,20
0.0305	15,90	2,82	2,83	15,95	15,85	2823	2826	2826	2829	0,007	0,23
0.0354	16,94	2,77	2,79	16,99	16,89	2784	2788	2788	2791	0,008	0,27
0.0404	18,06	2,71	2,75	18,11	18,01	2737	2741	2741	2746	0,009	0,32
0.0454	18,96	2,65	2,70	19,01	18,91	2696	2700	2701	2705	0,010	0,37
0.0504	20,47	2,58	2,63	20,52	20,42	2618	2624	2625	2630	0,012	0,45
0.0554	21,77	2,51	2,56	21,82	21,72	2544	2550	2551	2557	0,013	0,53
0.0604	23,11	2,44	2,47	23,16	23,06	2460	2467	2469	2475	0,015	0,62
0.0654	24,54	2,35	2,38	24,59	24,49	2362	2369	2372	2379	0,017	0,73
0.0704	26,05	2,27	2,27	26,10	26,00	2249	2256	2261	2268	0,020	0,86
0.0753	27,48	2,18	2,16	27,53	27,43	2134	2142	2147	2156	0,022	1,00
0.0803	28,90	2,08	2,04	28,95	28,85	2011	2020	2027	2035	0,024	1,17
0.0853	29,95	1,98	1,94	30,00	29,90	1916	1925	1933	1942	0,026	1,32
0.0903	31,28	1,88	1,82	31,33	31,23	1789	1799	1808	1818	0,028	1,52
0.0953	32,01	1,76	1,75	32,06	31,96	1717	1727	1737	1747	0,030	1,69
0.1003	32,37	1,65	1,71	32,42	32,32	1681	1691	1702	1711	0,031	1,85

on which the model is based.

Data availability statement

This research did not receive any specific grant from funding agencies in the public, commercial, or not-for-profit sectors.

Declaration of competing interest

The authors declare that they have no known competing financial interests or personal relationships that could have appeared to influence the work reported in this paper.

CRediT authorship contribution statement

F. Lo Savio: Conceptualization, Methodology, Investigation, Software. **G. La Rosa:** Conceptualization. **M. Bonfanti:** Conceptualization, Methodology, Validation.

Appendix

From the well-known criterion of distortion energy, the stress at the yield point is given by:

$$\sigma_{yp} = \sqrt{\sigma_1^2 + \sigma_2^2 + \sigma_3^2 - (\sigma_1\sigma_2 + \sigma_2\sigma_3 + \sigma_1\sigma_3)} \tag{A.1}$$

Eq. (A.1) allows defining the equivalent stress according to Von Mises (σ_{cr}) for the triaxial stress state to be compared with the admissible stress:

$$\sigma_{cr} = \sqrt{\frac{1}{2}\left[(\sigma_1 - \sigma_2)^2 + (\sigma_2 - \sigma_3)^2 + (\sigma_1 - \sigma_3)^2\right]} \tag{A.2}$$

In the case of uniaxial stress, the equivalent stress is reduced to:

$$\sigma_{cr}^{ua} = \sigma_1 \tag{A.3}$$

In the case of plane stress ($\sigma_3 = 0$) the equivalent stress is equal to:

$$\sigma_{cr} = \sqrt{\sigma_1^2 + \sigma_2^2 - \sigma_1\sigma_2} \tag{A.4}$$

and in the specific case of equibiaxial state ($\sigma_1 = \sigma_2 = \sigma_{eq}$):

$$\sigma_{cr}^{eq} = \sigma_{eq} \tag{A.5}$$

From equations (A.3) and (A.5), applying an equibiaxial stress equal to σ_1 is equivalent to applying a uniaxial stress equal to σ_1 (as in case of a tensile stress).

Appendix A. Supplementary data

Supplementary data to this article can be found online at https://doi.org/10.1016/j.polymertesting.2020.106548.

References

[1] M. Mooney, A theory of large elastic deformation, J. Appl. Phys. 11 (1940) 582–592, https://doi.org/10.1063/1.1712836.

[2] R.S. Rivlin, Large elastic deformations of isotropic materials IV. Further developments of the general theory, Phil. Trans. Roy. Soc. Lond. 241 (1948) 379–397, https://doi.org/10.1098/rsta.1948.0024.

[3] L.R.G. Treloar, The Physics of Rubber Elasticity, Clarendon Press, Oxford, 1975.

[4] E.M. Arruda, M.C. Boyce, A three-dimensional constitutive model for the large stretch behavior of rubber elastic materials, J. Mech. Phys. Solid. 41 (1993) 389–412, https://doi.org/10.1016/0022-5096(93)90013-6.

[5] O.H. Yeoh, Some forms of the strain energy function for rubber, Rubber Chem. Technol. 66 (1993) 754–771, https://doi.org/10.5254/1.3538343.

[6] R.W. Ogden, Non-Linear Elastic Deformations, Dover Publications, Mineola, N.Y., 1997, ISBN 978-0-486-69648-5.

[7] M. Sasso, G. Palmieri, G. Chiappini, D. Amodio, Characterization of hyperelastic rubber-like materials by biaxial and uniaxial stretching tests based on optical methods, Polym. Test. 27 (2008) 995–1004, https://doi.org/10.1016/j.polymertesting.2008.09.001.

[8] D.J. Charlton, J. Yang, K.K. Teh, A review of methods to characterize rubber elastic behavior for use in finite element analysis, Rubber Chem. Technol. 67 (1994) 481–503, https://doi.org/10.5254/1.3538686.

[9] M.K. Small, W.D. Nix, Analysis of the accuracy of the bulge test in determining the mechanical-properties of thin-films, J. Mater. Res. 7 (1992) 1553–1563, https://doi.org/10.1557/JMR.1992.1553.

[10] G. Gutscher, H.C. Wu, G. Ngaile, T. Altan, Determination of flow stress for sheet metal forming using the viscous pressure bulge (VPB) test, J. Mater. Process. Technol. 146 (2004) 1–7, https://doi.org/10.1016/S0924-0136(03)00838-0.

[11] M. Koç, E. Billur, Ö.N. Cora, An experimental study on the comparative assessment of hydraulic bulge test analysis methods, Mater. Des. 32 (2011) 272–281, https://doi.org/10.1016/j.matdes.2010.05.057.

[12] S.A. Aksenov, D. Sorgente, Investigation of stress-strain behavior of a sheet material using free bulging test, Procedia Eng 207 (2017) 1892–1897, https://doi.org/10.1016/j.proeng.2017.10.957.

[13] L. Vitu, N. Laforge, P. Malécot, N. Boudeau, S. Manov, M. Milesi, Characterization of zinc alloy by sheet bulging test with analytical models and digital image correlation, in: Proceedings of the 21st International Esaform Conference on Material Forming, AIP Conference Proceedings, Palermo, Italy, 2018, https://doi.org/10.1063/1.5035022.

[14] A. Dimarn, C. Thanadngarn, V. Buakaew, Y. Neamsup, Mechanical properties testing of sheet metal by hydraulic bulge test, in: Proceedings Vol. 9234, International Conference on Experimental Mechanics 2013 and Twelfth Asian Conference on Experimental Mechanics, 2014, https://doi.org/10.1117/12.2054257.

[15] T. Tsakalakos, The bulge test: a comparison of theory and experiment for isotropic and anisotropic films, Thin Solid Films 75 (1981) 293–305, https://doi.org/10.1016/0040-6090(81)90407-7.

[16] J. Diani, M. Brieu, J.M. Vacherand, A. Rezgui, Directional model for isotropic and anisotropic hyperelastic rubber-like materials, Mech. Mater. 36 (2004) 313–321, https://doi.org/10.1016/S0167-6636(03)00025-5.

[17] M. Calì, F. Lo Savio, Accurate 3D reconstruction of a rubber membrane inflated during a Bulge Test to evaluate anisotropy, in: Advances on Mechanics, Design Engineering and Manufacturing - Lecture Notes in Mechanical Engineering, Springer, 2017, pp. 1221–1231, https://doi.org/10.1007/978-3-319-45781-9_122.

[18] E.W. Ross Jr., W. Prager, On the theory of the bulge test, Q. Appl. Math. 12 (1954) 86–91.

[19] M. Sigvant, K. Mattiasson, H. Vegter, P. Thilderkvist, A viscous pressure bulge test for the determination of a plastic hardening curve and equibiaxial material data, Int. J. Material Form. 2 (2009) 235–242, https://doi.org/10.1007/s12289-009-0407-y.

[20] R. Hill, A theory of the plastic bulging of a metal diaphragm by lateral pressure, London Edinburgh Dublin Phil. Mag. J. Sci.: Series 7 (1950) 1133–1142, https://doi.org/10.1080/14786445008561154, 41.

[21] F. Jovane, An approximate analysis of the superplastic forming of a thin circular diaphragm: theory and experiments, Int. J. Mech. Sci. 10 (1968) 405–427, https://doi.org/10.1016/0020-7403(68)90005-2.

[22] Z. Marciniak, Limit Deformations in Sheet Metal Stamping (In Polish), Wydaw. Nauk.-Techn., Warszawa, 1971.

[23] J. Chakrabarty, J.M. Alexander, Hydrostatic bulging of circular diaphragms, J. Strain Anal. Eng. Des. 5 (1970) 155–161, https://doi.org/10.1243/03093247V053155.

[24] H.M. Shang, V.P.W. Shim, A model study of the effect of the size of the die shoulder in hydroforming, J. Mech. Work. Technol. 10 (1984) 307–323, https://doi.org/10.1016/0378-3804(84)90046-9.

[25] M. Atkinson, An approximate explicit solution for polar strain of hydraulically bulged circular diaphragms, Trans. ASME J. Vib. Acoust. Stress Reliab. Des. 109 (1987) 192–195, https://doi.org/10.1115/1.3269413.

[26] Z.X. Guo, N. Ridley, Modelling of superplastic bulge forming of domes, Mater. Sci. Eng., A 114 (1989) 97–104, https://doi.org/10.1016/0921-5093(89)90849-6.

[27] A.A. Kruglov, F.U. Enikeev, R.Y. Lutfullin, Superplastic forming of a spherical shell out a welded envelope, Mater. Sci. Eng., A 323 (2002) 416–426, https://doi.org/10.1016/S0921-5093(01)01376-4.

[28] H. Campos, A.D. Santos, B. Martins, F. Barlat, Hydraulic Bulge Test for Stress-Strain Curve Determination and Damage Calibration for Ito-Goya Model, World Congress on Computational Mechanics XI, Barcelona, 2014.

[29] A.D. Santos, J.G. Mendes, F. Gomes Almeida, P. Teixeira, M.S. Li, A. Barata da Rocha, Developing a Bulge Tester for Sheet Metal Stress-Strain Determination, 3rd International Conference on Integrity, Reliability and Failure, Porto, 2009.

[30] J. Kána, B. Mašek, Š. Jeníček, A. Ronešová, Apparatus for bulge testing metal foils using a laser scanner, Procedia Eng 69 (2014) 1029–1032, https://doi.org/10.1016/j.proeng.2014.03.086.

[31] M. Calì, R. Ambu, Advanced 3D photogrammetric surface reconstruction of extensive objects by UAV camera image acquisition, Sensors 18 (2018) 2815, https://doi.org/10.3390/s18092815.

[32] A.H. Choi, S. Akyol, A. Bendavid, B. Ben-Nissan, Nanobioceramic Thin Films: Surface Modifications and Cellular Responses on Titanium Implants, Titanium in Medical and Dental Applications, Woodhead Publishing Series in Biomaterials, 2018, pp. 147–173, https://doi.org/10.1016/B978-0-12-812456-7.00007-X.

[33] W.G. Knauss Chasiotis, Experimentation at the micron- and submicron scale, vol. 8: interfacial and nanoscale fracture, in: Comprehensive Structural Integrity, 2003, https://doi.org/10.1016/B0-08-043749-4/08038-1.

[34] J. Holzer, T. Pikálek, Z. Buchta, L. Josef, H.A. Tinoco, A. Chlupová, T. Kruml, Development of the Bulge Test Equipment for Measuring Mechanical Properties of Thin Films, 26th International Conference on Metallurgy and Materials, 2017. Brno.

[35] G. Montay, M. François, M. Tourneix, B. Guelorget, C. Vial-Edwards, I. Lira, Strain and strain rate measurement during the bulge test by electronic speckle pattern interferometry, J. Mater. Process. Technol. 184 (2007) 428–435, https://doi.org/10.1016/j.jmatprotec.2006.12.013.

[36] E.P. Marinho, A.M. Silva Jr., G.F. Batalha, Comparison between direct and indirect measurement methods for bulge tests, Arch. Mater. Sci. Eng. 61 (2013) 77–86.

[37] G. Machado, D. Favier, G. Chagnon, Jerrams, Murphy, From the experimental determination of stress-strain full fields during a bulge test thanks to 3D-DIC technique to the characterization of anisotropic Mullins effect, in: Constitutive Models for Rubber VII, 2012, ISBN 978-0-415-68389-0. London.

[38] C. Feichter, Z. Major, R.W. Lang, Methods for measuring biaxial deformation on rubber and polypropylene specimens, in: E.E. Gdoutos (Ed.), Experimental Analysis of Nano and Engineering Materials and Structures, 2007, pp. 273–274, https://doi.org/10.1007/978-1-4020-6239-1_135.

[39] J. Neggers, J.P.M. Hoefnagels, F. Hild, S. Roux, M.G.D. Geers, Global digital image correlation for pressure-deflected membranes, in: G.A. Shaw, B.C. Prorok, L.-V. A. Starman (Eds.), Proceedings of the 2012 Annual Conference on Experimental and Applied Mechanics vol. 6, Springer, New York, 2012, pp. 135–140, https://doi.org/10.1007/978-1-4614-4436-7_20.

[40] F. Lo Savio, G. Capizzi, G. La Rosa, G. Lo Sciuto, Creep assessment in hyperelastic material by a 3D Neural Network Reconstructor using bulge testing, Polym. Test. 63 (2017) 65–72, https://doi.org/10.1016/j.polymertesting.2017.08.009.

[41] L.R.G. Treloar, Strains in an inflated rubber sheet, and the mechanism of bursting, Rubber Chem. Technol. 17 (1944) 957–967, https://doi.org/10.5254/1.3546716.

[42] N. Reuge, F.M. Schmidt, Y. Le Maoult, M. Rachik, F. Abbé, Elastomer biaxial characterization using bubble inflation technique. I: experimental investigations, Polym. Eng. Sci. 41 (2001) 522–531, https://doi.org/10.1002/pen.10749.

[43] N. Reuge, F.M. Schmidt, Y. Le Maoult, M. Rachik, F. Abbé, Elastomer biaxial characterization using bubble inflation technique. II: numerical investigation of some constitutive models, Polym. Eng. Sci. 41 (2001) 532–541, https://doi.org/10.1002/pen.10750.

[44] M.N. Charalambides, L. Wanigasooriya, G.J. Williams, S. Chakrabarti, Biaxial deformation of dough using the bubble inflation technique. I. Experimental, Rheol. Acta 41 (2002) 532–540, https://doi.org/10.1007/s00397-002-0242-2.

[45] J.Y. Sheng, L.Y. Zhang, B. Li, G.F. Wang, X.Q. Feng, Bulge test method for measuring the hyperelastic parameters of soft membranes, Acta Mech. 228 (2017) 4187–4197, https://doi.org/10.1007/s00707-017-1945-x.

[46] Z. Marciniak, J.L. Duncan, S.J. Hu, Mechanics of Sheet Metal Forming, Butterworth-Heinemann Ed., Oxford, 2002, https://doi.org/10.1016/B978-0-7506-5300-8.X5000-6.

[47] Z. Śloderbach, Conditions of stability loss during the test of hydraulic forming of drawpieces, Part I. Derivation of basic equations and relationships, Int. J. Appl. Mech. Eng. 20 (2015) 917–938, https://doi.org/10.1515/ijame-2015-0059.

[48] J. Slota, E. Spišák, Determination of flow stress by the hydraulic bulge test, Metalurgija 47 (2008) 13–17. https://hrcak.srce.hr/17784.

[49] R.W. Ogden, Volume changes associated with the deformation of rubber-like solids, J. Mech. Phys. Solid. 24 (1976) 323–338, https://doi.org/10.1016/0022-5096(76)90007-7.

[50] H. Kobayashi, R. Vanderby, New strain energy function for acoustoelastic analysis of dilatational waves in nearly incompressible, hyper-elastic materials, J. Appl. Mech. 72 (2005) 843–851, https://doi.org/10.1115/1.2041661.

[51] F. Lo Savio, M. Bonfanti, G.M. Grasso, D. Alizzio, An experimental apparatus to evaluate the non-linearity of the acoustoelastic effect in rubber-like materials, Polym. Test. 80 (2019), 106133, https://doi.org/10.1016/j.polymertesting.2019.106133. In press.

[52] F. Lo Savio, M. Bonfanti, A novel device for measuring the ultrasonic wave velocity and the thickness of hyperelastic materials under quasi-static deformations, Polym. Test. 74 (2019) 235–244, https://doi.org/10.1016/j.polymertesting.2019.01.005.

[53] G.R. Hamed, B.H. Park, The mechanism of carbon black reinforcement of SBR and NR vulcanizates, Rubber Chem. Technol. 72 (1999) 946–959, https://doi.org/10.5254/1.3538844.

[54] S.S. Choi, B.H. Park, H. Song, Influence of filler type and content on properties of styrene-butadiene rubber (SBR) compound reinforced with carbon black or silica, Polym. Adv. Technol. 15 (2004) 122–127, https://doi.org/10.1002/pat.421.

[55] M. Heydari-Meybodi, M.R. Ayatollahi, F. Berto, Rupture analysis of rubber in the presence of a sharp V-shape notch under pure mode-I loading, Int. J. Mech. Sci. 146–147 (2018) 405–415, https://doi.org/10.1016/j.ijmecsci.2018.08.008.

[56] S.M. Hosseini, M. Razzaghi-Kashani, Catalytic and networking effects of carbon black on the kinetics and conversion of sulfur vulcanization in styrene butadiene rubber, Soft Matter 14 (2018) 9194–9208, https://doi.org/10.1039/c8sm01953c.
[57] R.A. Toupin, B. Bernstein, Sound waves in deformed perfectly elastic materials. Acoustoelastic effect, J. Acoust. Soc. Am. 33 (1961) 216–225, https://doi.org/10.1121/1.1908623.
[58] G.C. Johnson, Acoustoelastic theory for elastic-plastic materials, J. Acoust. Soc. Am. 70 (1998) 591–595, https://doi.org/10.1121/1.386748.
[59] Z. Abiza, M. Destrade, R.W. Ogden, Large acoustoelastic effect, Wave Motion 49 (2012) 364–374, https://doi.org/10.1016/j.wavemoti.2011.12.002.
[60] I.Y. Kuo, B. Hete, K.K. Shung, A novel method for the measurement of acoustic speed, J. Acoust. Soc. Am. 88 (1990) 1679–1682, https://doi.org/10.1121/1.400242.
[61] D.K. Hsu, M.S. Hughes, Simultaneous ultrasonic velocity and sample thickness measurement and application in composites, J. Acoust. Soc. Am. 92 (1992) 669–675, https://doi.org/10.1121/1.405279.
[62] Y.H. Kim, S. Sung-Jin, L. Jeong-Ki, Simultaneous measurements of the ultrasonic wave velocity and thickness of a solid plate made from one side of the plate, Meas. Sci. Technol. 14 (2003) 13–16, https://doi.org/10.1088/0957-0233/14/5/401.
[63] N. Bilaniuk, G.S.K. Wong, Speed of sound in pure water as a function of temperature, J. Acoust. Soc. Am. 93 (1993) 1609–1612, https://doi.org/10.1121/1.406819.
[64] Z. Zhang, A flexible new technique for camera calibration, IEEE T Pattern Anal 22 (2000) 1330–1334, https://doi.org/10.1109/34.888718.